Article

Cell

Structure of Mammalian Respiratory Supercomplex $I_1III_2IV_1$

Graphical Abstract

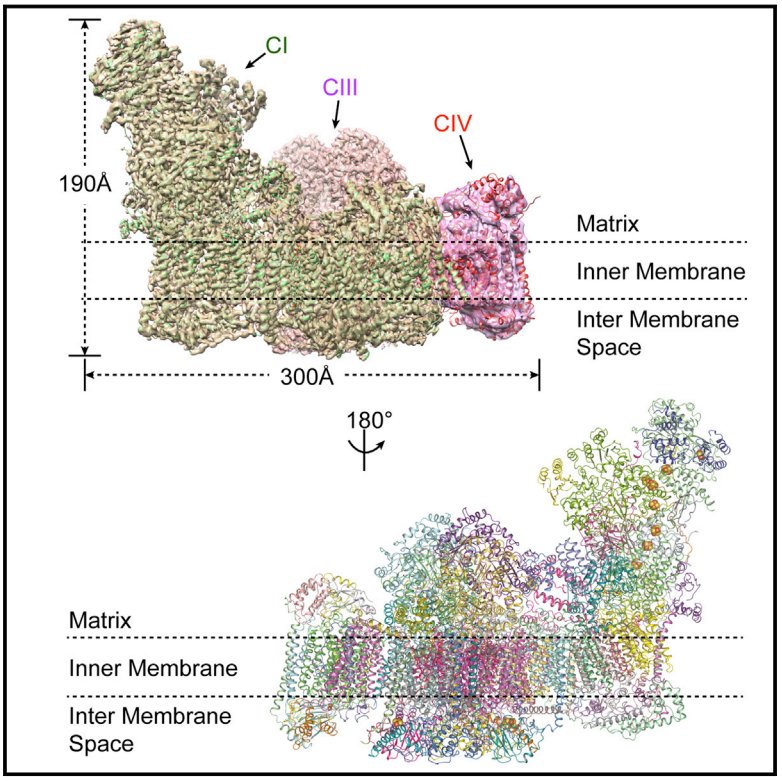

Highlights

- The structure of respiratory supercomplex $I_1III_2IV_1$ was determined at 4.0 Å resolution
- The atomic structure of complex I and III with side chains at 3.6 Å resolution
- Phospholipid molecules mediate the supercomplex arrangement
- Provided an alternative electron transfer mechanism

Authors

Meng Wu, Jinke Gu, Runyu Guo, Yushen Huang, Maojun Yang

Correspondence

maojunyang@tsinghua.edu.cn

In Brief

A 4.0-Å structure of the mammalian respiratory supercomplex suggests a new electron transfer mechanism and provides detailed insights into how the subunits come together.

Wu et al., 2016, Cell *167*, 1598–1609
December 1, 2016
http://dx.doi.org/10.1016/j.cell.2016.11.012

CellPress

Cell

Article

Structure of Mammalian Respiratory Supercomplex $I_1III_2IV_1$

Meng Wu,[1,2] Jinke Gu,[1,2] Runyu Guo,[1,2] Yushen Huang,[1,2] and Maojun Yang[1,3,*]
[1]Ministry of Education Key Laboratory of Protein Science, Tsinghua-Peking Joint Center for Life Sciences, Beijing Advanced Innovation Center for Structural Biology, School of Life Sciences, Tsinghua University, Beijing 100084, China
[2]Co-first author
[3]Lead Contact
*Correspondence: maojunyang@tsinghua.edu.cn
http://dx.doi.org/10.1016/j.cell.2016.11.012

SUMMARY

The mammalian respiratory chain complexes assemble into supercomplexes (SCs) and reside in the inner mitochondrial membrane to transfer electrons and establish the proton gradient for complex V to synthesize ATP. The precise arrangement of SCs is largely unknown. Here, we report a 4.0-Å cryo-electron microscopy (cryo-EM) structure of the major SC in porcine heart, the 1.7-MDa $SCI_1III_2IV_1$. The complex III (CIII) dimer and complex IV (CIV) bind at the same side of the L-shaped complex I (CI). Several accessory or supernumerary subunits of CI, such as NDUFA11, NDUFB4, NDUFB8, and NDUFB9, directly contribute to the oligomerization of CI, CIII, and CIV. COX7C and COX7A of CIV attach CIV to the concave surface formed by CIII and the distal end of membrane arm of CI. The structure suggests a possible mechanism by which electrons are transferred from NADH to cytochrome *c* and provides a platform for future functional dissection of respiration.

INTRODUCTION

In animals, the energy contained in organic compounds can be released via specific metabolic pathways to generate ATP by the oxidative phosphorylation (OXPHOS) system via a unique mechanism termed chemiosmosis (Acín-Pérez et al., 2004). In mammals, the OXPHOS system in mitochondria is composed of three types of proton-pumping complexes, electron carrier pools, non-proton-pumping complex II and various complex-II-like auxiliary electron donors, and ATP synthase (Acín-Pérez et al., 2008). Decades of extensive structural and functional investigations have depicted a general picture of how these large proton-pumping complexes could perform their duties. Respiratory complex I (CI; NADH:ubiquinone oxidoreductase), consisting of 44 different subunits with a total molecular weight of ~980 kDa, can transfer two electrons from NADH to ubiquinone and simultaneously pump four protons from the mitochondrial matrix to the intermembrane space (IMS) in a single cycle (Althoff et al., 2011). Respiratory complex III (CIII; cytochrome bc_1 complex), functioning as a dimer with each 240 kDa monomer containing 11 subunits, transfers two electrons from the QH_2 provided by CI or CII-like enzymes to two cytochrome *c* (Cyt.*c*) molecules while pumping two protons from the matrix to the IMS (Belevich et al., 2007). Respiratory complex IV (CIV; cytochrome *c* oxidase), existing as a 210-kDa monomer with 14 subunits, delivers four electrons from four Cyt.*c* molecules to one oxygen molecule, forming two water molecules, and pumping four protons into IMS at the same time (Benard et al., 2008). The proton-pumping-coupled electron transfer reactions are shown below (Sazanov, 2015):

$$\mathrm{CI: NADH + H^+ + Q + 4H^+(matrix) \rightarrow NAD^+ + QH_2 + 4H^+(IMS)}$$

$$\mathrm{CIII: 2Cyt.}c\mathrm{(oxidized) + QH_2 + 2H^+(matrix) \rightarrow 2Cyt.}c\mathrm{(reduced) + Q + 4H^+(IMS)}$$

$$\mathrm{CIV: 4Cyt.}c\mathrm{(reduced) + 8H^+(matrix) + O_2 \rightarrow 4Cyt.}c\mathrm{(oxidized) + 2H_2O + 4H^+(IMS)}$$

Since Shägger and his colleagues identified the respiratory supercomplexes (SCs) via blue native PAGE (BN-PAGE) (Schägger and Pfeiffer, 2000), an exciting concept of the organization of respiratory chain complexes has emerged, i.e., individual respiratory complexes can further assemble into different types of SCs (Blaza et al., 2014). The SCs containing CI, CIII dimer, and different copy numbers of CIV, which are capable to performing respiratory reactions, are also called the respirasomes. The distribution of various SC types in living organisms can vary depending on tissue types and cell conditions, such as the level of energy demands (Acín-Pérez et al., 2008). The specific correlation between SC distribution types and cell conditions calls for further investigation.

Introduction of the SC concept led to intensive studies revealing the biological significance of forming an SC organization in OXPHOS. First, the assembly of CIII and CIV into CI can promote the assembly and stability of CI (Enríquez, 2016; Genova, 2014; Hirst, 2013; Lamantea et al., 2002). Second, the formation of SCs can significantly reduce the generation of reactive oxygen species (ROS) (Lapuente-Brun et al., 2013; Maranzana et al., 2013). Third, SCs can enhance the catalytic activity of individual components (Mitchell, 1961; Moreno-Lastres et al., 2012). Fourth, SCs can raise the efficiency of electron transfer through substrate channeling (Schäfer et al., 2006; Schägger

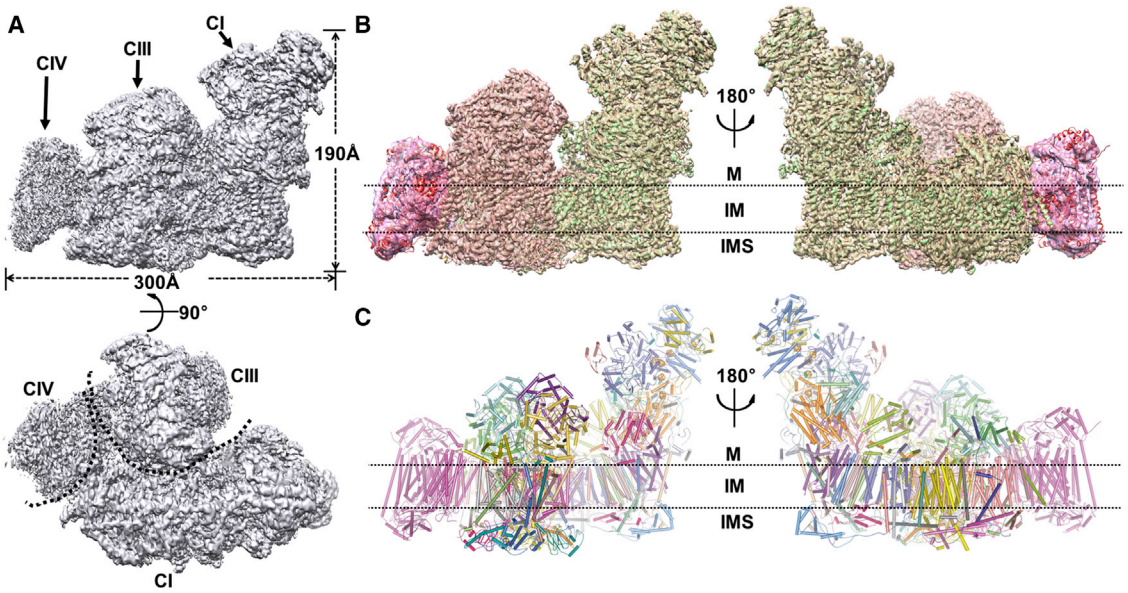

Figure 1. Overall Structure of $SCI_1III_2IV_1$

(A) The side views along the membrane of the density map of $SCI_1III_2IV_1$ at 4.0 Å (at 7σ contour level), with distinct regions labeled and indicated by black arrows. The bottom view from the intermembrane side of the map. The black dashed lines indicate the boundary of the three complexes. CI, complex I; CIII, complex III; CIV, complex IV.

(B) The CI, CIII, and CIV maps with the cartoon presented models after soft mask subregion refinement were aligned to the 4.0-Å map (7σ contour level of CI and CIII; 5σ contour level of CIV) and are shown in two differently rotated views along the membrane. The structural models of CI, CIII, and CIV are colored in green, wheat, and magenta, respectively. The transmembrane region is indicated by two dashed lines. M, matrix; IM, inner membrane; IMS, intermembrane space.

(C) The overall structure of $SCI_1III_2IV_1$. Different subunits of CI and CIII are shown in different colors, and CIV is colored in magenta.

See also Figures S1 and S2.

and Pfeiffer, 2000; Smirnov and Nori, 2012). Despite decades of structural studies on CI, CIII, and CIV (Baradaran et al., 2013; Efremov et al., 2010; Efremov and Sazanov, 2011; Guo et al., 2016; Hunte et al., 2010; Sazanov and Hinchliffe, 2006; Tsukihara et al., 1995, 1996; Vinothkumar et al., 2014; Zhang et al., 1998; Zhu et al., 2016), only low-resolution structures of SC have been available until now (Althoff et al., 2011; Dudkina et al., 2011; Gu et al., 2016; Letts et al., 2016; Schäfer et al., 2007), limiting our mechanistic understanding of these observations. In the present study, using single-particle cryo-electron microscopy (cryo-EM) and a sub-region refinement method, we obtained the structure of mammalian $SCI_1III_2IV_1$ at near-atomic resolution. Our structure not only reveals the precise arrangement of CI, CIII, and CIV but also suggests possible mechanisms by which electrons are transferred from NADH to Cyt.*c*.

RESULTS

Structure Determination and Overall Structure of $SCI_1III_2IV_1$

The 1.7-MDa $SCI_1III_2IV_1$ was solubilized with digitonin from porcine hearts and purified to apparent homogeneity for final sample preparation and structural determination as previously described (Gu et al., 2016) (Figure S1A). After 2D and 3D classification of 424,000 particles, 162,000 particles were subjected to high-resolution refinement, resulting in a 3D density map with an overall resolution of 4.0 Å by the "gold standard" Fourier shell correlation (FSC) = 0.143 criterion (Figures 1A and S1B–S1G). The density map can be clearly divided into three parts corresponding to CI, CIII, and CIV (Figure 1A). Sub-region refinement with step-by-step reduction of the soft masks corresponding to SCI_1III_2, CI, CIII dimer, and CIV results in further improvement of the density maps to 3.9, 3.6, 3.6, and 6.4 Å, respectively (gold-standard FSC = 0.143 criterion) (Figures S1D and S2). Subsequent docking of the cryo-EM maps and models of CI (PDB: 5GPN) (Gu et al., 2016), CIII (PDB: 1BGY) (Iwata et al., 1998), and CIV (PDB: 1OCC) (Tsukihara et al., 1996) into the 4.0-Å $SCI_1III_2IV_1$ map resulted in high correlation coefficients. The CI and CIII models were further optimized manually with Coot (Emsley and Cowtan, 2004) (Figures 1B, 1C, and S2), and real-space refinement was performed with Phenix (Adams et al., 2002).

The mammalian respiratory $SCI_1III_2IV_1$ is the largest and most complicated enzyme in the inner mitochondrial membrane. It has a dimension of ~190 Å in height and 300 Å in length (Figure 1A). The 3.6-Å density maps of CI and CIII alone allowed us to build the model with side chains clearly visible for the majority of residues from all subunits, except NDUFA12 and NDUFV3 of CI. The two-fold axis of the CIII dimer is oriented perpendicularly to the membrane arm of CI (Figure 1). The rectangular density of CIV monomer was positioned at the distal end of the membrane arm of CI and was adjacent to the CIII dimer, and we assigned the CIV monomer (PDB: 1OCC) (Tsukihara et al., 1996) into the 6.4-Å map (Figures 1B and 1C). In the SC structures, the density for the side chains was well resolved in the tightly packed

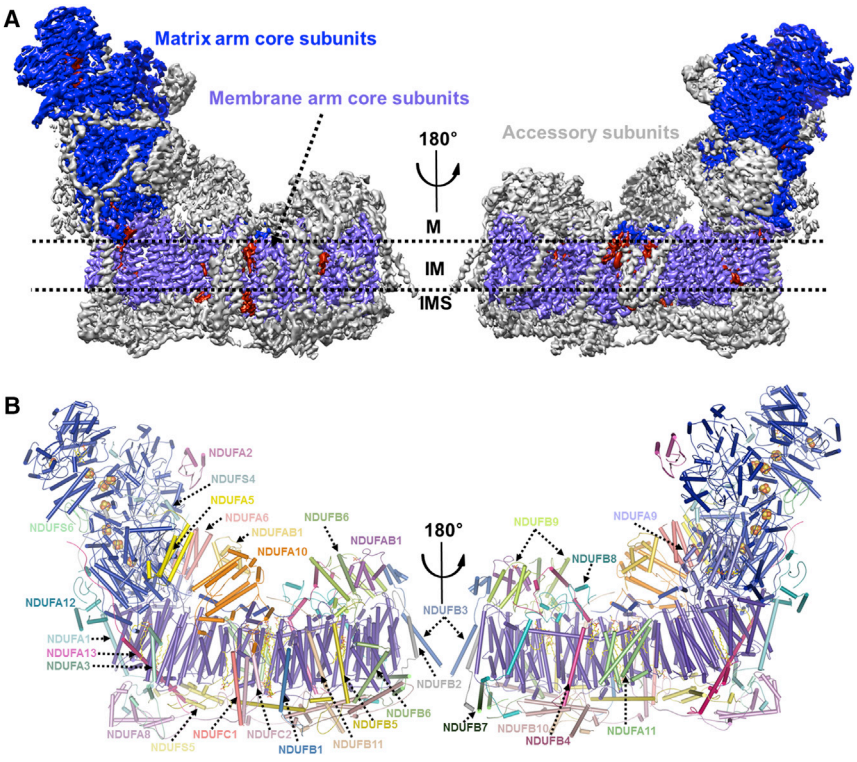

Figure 2. Overall Structure of CI

(A) The overall density map of CI. The side views along the membrane of the sharpened map filtered to a resolution of 3.6 Å (7σ contour level) in two differently rotated views along the membrane. The matrix arm core subunits are shown in blue, while core subunits of the membrane arm are shown in slate. Accessory subunits are shown in gray, and the co-factors and phospholipids are shown in red. The transmembrane region is indicated by two dashed lines. M, matrix; IM, inner membrane; IMS, intermembrane space.

(B) The overall structure of CI. Cartoon representation of the CI structure in two differently rotated views along the membrane. The matrix and membrane arms core subunits are colored in blue and slate, respectively. The supernumerary subunits are colored as labeled with texts in the same colors, respectively. The FeS-clusters are shown as spheres. The phospholipids are shown as yellow sticks.

See also Figures S2, S3, S4, S5, and S6.

subunits, while the ones at the distal end of the peripheral regions were resolved at a relatively lower resolution due to their less ordered conformation (Figures 1B and S2).

In the structure, we were able to accurately place 14 core subunits and 30 supernumerary subunits in CI, 22 subunits in CIII, and do rigid body fit of the 13 subunits in CIV (Figures 1C and S3A). In total, the structure of CI contains 44 subunits with 78 transmembrane helices (TMHs) (60 from the core subunits and 18 from the supernumerary subunits). CIII contains 22 subunits with 26 TMHs, and CIV has 13 subunits with 28 TMHs. We also located 11 and 12 phospholipids in CI and CIII and 6 and 2 heme molecules in CIII and CIV, respectively (Figures 1C and S3).

Structure of CI

The overall structure of CI is ~190 Å in height and 250 Å in length. Out of the 45 subunits (two copies of NDUFAB1) of CI, 44 subunits were assigned in the 3.6-Å-resolution density map. The existence of NDUFV3 could not be detected which might be due to the flexibility (Figure 2; Table S1). Almost all residues were modeled into the structure, except residues of NDUFA12, due to their relatively poor density quality (Figures 2A and S4; Table S1). It was reported that the 14 conserved core subunits of CI form an L-shaped structure (Baradaran et al., 2013; Berrisford et al., 2016; Efremov et al., 2010; Efremov and Sazanov, 2011; Vinothkumar et al., 2014; Zhu et al., 2016), which catalyzes the energy transducing reactions. The seven matrix domain core subunits, surrounded by ten supernumerary subunits, protrude out of the membrane to form the matrix arm. The seven membrane arm core subunits are buried in the mitochondrial inner membrane. 21 additional supernumerary subunits encircle this core, and 14 of these supernumerary components have at least one TM domain each (Figures 2B and S4; Table S1). More interestingly, in addition to the 44 polypeptides, the density also allowed us to assign an flavin mononucleotide (FMN) molecule in NDUFV1, eight FeS clusters for the electron transfer cascade in the matrix region, an NADPH molecule in NDUFA9, a Zn^{2+} ion in NDUFS6, two decanoyl (C10)-4′-phosphopantetheine (D4PP) group in two acyl carrier protein complexes (NDUFAB1-NDUFA6, and NDUFAB1-NDUFB9) (Figures S5A–S5D), three phosphatidylcholines (PCs), four phosphatidylethanolamines (PEs), and four cardiolipins in the membrane arm (Figure S3). Together, the overall structure of CI is shaped like a "foot" in a "sandal," in which the L-shaped 14 core subunits form a foot slipping into a sandal-like cage packed by the 30 supernumerary subunits (Figure 2).

Consistent with previous studies (Brandt, 2006; Hunte et al., 2010), CI can be divided into four functional modules. The distal half of the matrix arm, comprising the NDUFV1, NDUFV2, and NDUFS1 core subunits and the NDUFA2, NDUFS4, and NDUFS6 accessory subunits, forms the M_D module that contains five FeS clusters and an FMN molecule to oxidize NADH (Figure 3A). The proximal half of the matrix arm (M_P) also contains three FeS clusters and comprises the NDUFS2, NDUFS3, NDUFS7, and NDUFS8 core subunits, together with the NDUFA5, NDUFA6, NDUFA7, NDUFA9, NDUFA12, and NDUFAB1 supernumerary subunits. The M_P module docks onto the membrane arm and contains a sealed ubiquinone-binding chamber (Q-chamber), which is mainly formed by the NDUFS2, NDUFS7, and ND1 subunits from the membrane arm and is used to reduce ubiquinone near the N2 FeS cluster (Zickermann et al., 2015) (Figures 2B, 3A, and 3B). The membrane arm of CI comprises seven mitochondrial-encoded membrane core subunits, which is 180 Å in length along the membrane with a slightly bent shape. The membrane

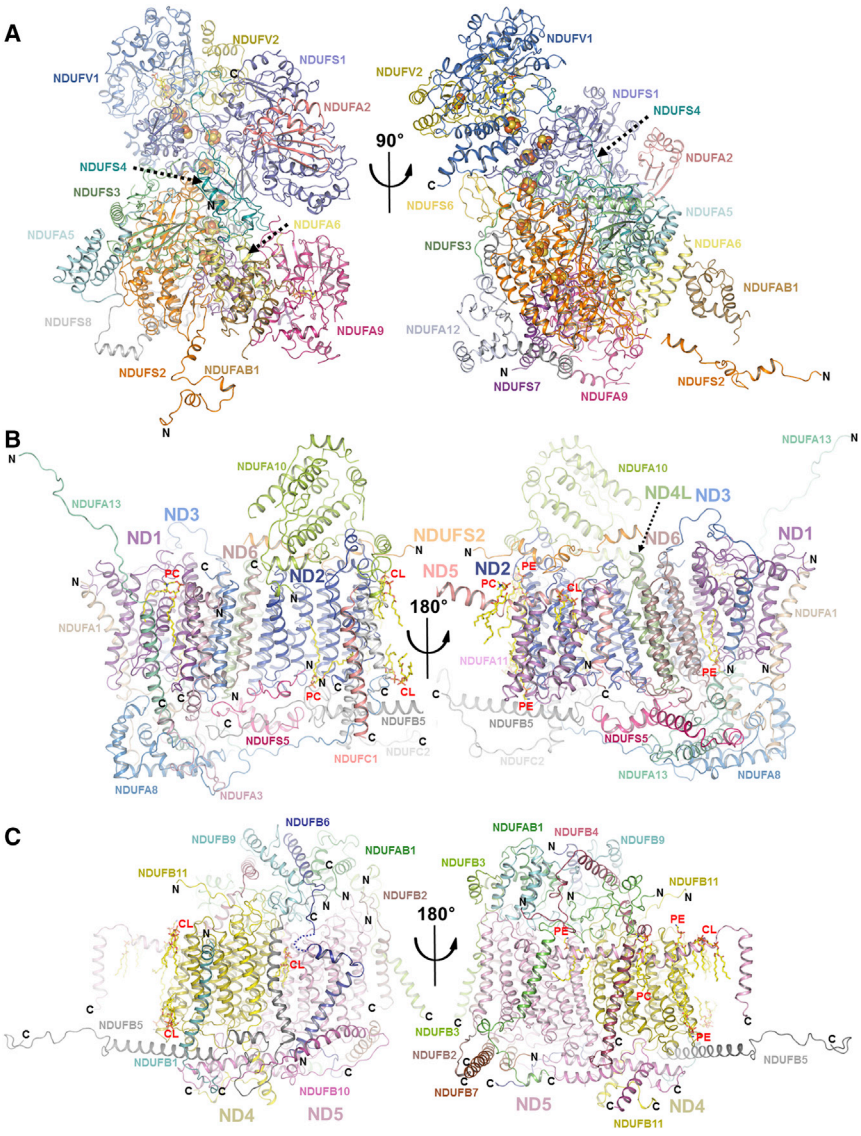

Figure 3. Structure of the Matrix Arm, P_P, and P_D Modules of CI

(A) The overall structure of the matrix arm. Cartoon representation of the matrix arm in two differently rotated views. 16 subunits, including 7 core subunits and 9 supernumerary subunits, are colored as labeled with text in the same colors, respectively. The FeS-clusters are shown as spheres.

(B) The overall structure of the P_P module. Cartoon representation of the P_P module structure in two differently rotated views along the membrane. The subunits are colored as labeled with text in the same colors, respectively. The phospholipids are shown in yellow sticks. The N and C termini are indicated. CL, cardiolipin; PC, phosphatidylcholine; PE, phosphatidylethanolamine.

(C) The overall structure of the P_D module. Cartoon representation of the P_D module structure in two differently rotated views along the membrane. The subunits are colored as labeled with text in the same colors, respectively. The phospholipid molecules are shown as yellow sticks. The N and C termini are indicated.

See also Figure S6.

arm contains 21 nuclear-encoded supernumerary components, in which four of them contain CX9C motifs that form the intramolecular disulphides within the "CHCH" domains (NDUFA8, NDUFS5, NDUFB7, and NDUFB10) (Figure S4) are located at the intermembrane side and three subunits (NDUFA10, NDUFAB1b and NDUFB9) sit on the membrane arm at the matrix side (Figure 2B). 12 of the 21 accessory subunits contain a single TMH, NDUFC2 contains two TMHs, and NDUFA11 has four TMHs. Interestingly, the C termini of all of these proteins are located in IMS (Figure S6A). Previous studies suggested that the orientation preference of these proteins might be determined during their translocation from cytoplasm to mitochondria (Chacinska et al., 2009; Schmidt et al., 2010). The core subunits ND5 and ND4, together with NDUFB1-11 and NDUFAB1 supernumerary components, constitute the P_D module, containing the two distal antiporter-like proton pumps (Figure 3C). The core subunits ND1, ND2, ND3, ND4L, and ND6, together with NDUFA1, NDUFA3, NDUFA8, NDUFA10, NDUFA11, NDUFA13, NDUFS5, NDUFC1, and NDUFC2 supernumerary subunits, constitute the proximal pump module (P_P), which contains another two antiporter-like proton pumps and links the matrix arm with the membrane arm (Figures 2B and 3B).

Conformational Change between CI and CIII

3D classification reveals that the particles used to refine the SC structure can be divided into two major groups. Each group contains ~80,000 particles, and their maps are refined to ~4.5 Å (Figure S1D). Interestingly, although the membrane arms of the two structures in both states are indistinguishable (Figures 4A–4C), the matrix arms of CI and the overall structures of CIII show significant conformational changes (Figure 4D). In one state, the matrix arms of CI and CIII move closer to each other, forming a tighter SC state than the other state (Figures 4A and 4B). The large conformational changes of the matrix arms in CI suggest the existence of different conformational states during the electron transfer processes.

Interaction between the Complexes

There are three accessory proteins (NDUFB4, NDUFB8, and NDUFA11) lining in the middle of CI and CIII (Figure 5A). Both NDUFB4 and NDUFB8 are single TMH proteins with their N termini intertwined to form a complex on the matrix side. The N-terminal loop of NDUFB4, together with the following two helices, forms a U-shaped structure to cover the loop-rich structure at the N terminus of NDUFB8 (Figure 5A). The TMHs of NDUFB4

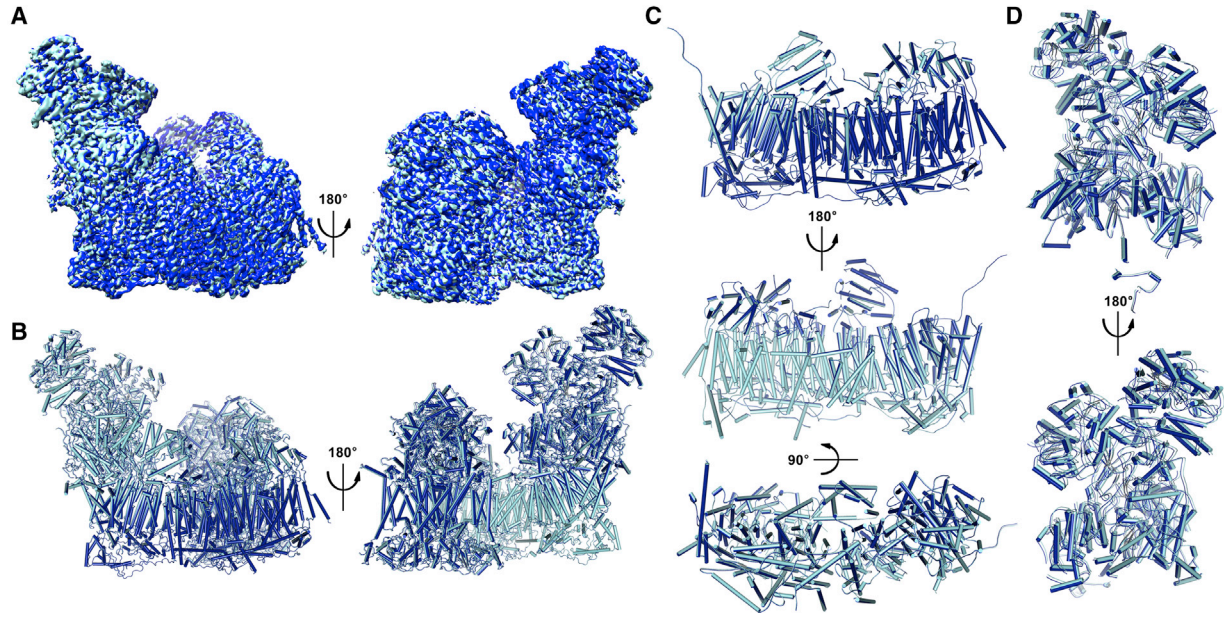

Figure 4. Conformational Change between CI and CIII

(A) Comparison of the two states density maps of SCI_1III_2 with 4.5 and 4.6 Å resolutions (at 8σ contour level). The marine and cyan density maps stand for two state of SCI_1III_2. These maps are shown in two differently rotated views along the membrane. The distance between CI matrix arm and CIII of the marine map is closer than the cyan one.

(B) Comparison of the two states structure models. From the side view structure models, it is clear that the model colored marine is the tight one while the other is the loose one.

(C) The CI membrane arms of the two states have been superimposed and there are almost no conformational changes. The membrane arms are viewed from the side (along the membrane) and from the top (matrix side).

(D) The CI matrix arms of the two states are compared and have larger conformational changes than the membrane arms. The matrix arms are shown from the side.

See also Figure S1.

and NDUFB8 contact different regions of the $ND5^{HL}$ helix. Their other side (opposite the TMHs of CI) faces the gap between CI and CIII (Figure 5A).

NDUFA11 contains a bundle of four TMHs roughly in parallel with the TM helices in the middle of the core membrane arm of CI, with a short helix at the N terminus and a loop region at the C terminus (Figure 5A). Each TMH contains a cysteine residue, and $NDUFA11^{C95}$ and $NDUFA11^{C115}$ indeed form a disulfide bond. Although $NDUFA11^{C18}$ and $NDUFA11^{C75}$ are also close to each other, the density clearly shows that the side chains of these two cysteines point in different directions (Figures S5E and S5F), indicating that they do not form a covalent bond under our experimental conditions. The disulfide bond in the transmembrane region could potentially contribute to the stability of the overall structure of NDUFA11, and its biological function needs further characterization.

NDUFA11 interacts with multiple components, including ND2, NDUFB4, the long amphipathic helix (HL) and C-terminal TMH of ND5, and ND4 (Figure 5A). The N terminus and the TMH1 of NDUFA11 are close to the last TMH following the HL helix of ND5 to provide a series of interactions (Figures 5A and 5B). The C terminus of $NDUFA11^{TMH4}$ also makes contacts with the $ND4^{W190\ and\ F194}$ at the N terminus of $ND4^{TMH8}$, and the side chain of $NDUFA11^{E131}$ forms a hydrogen bond with the side chain of $ND4^{S189}$ to further stabilize the interaction. The C-terminal loop of NDUFA11 inserts into the groove formed by $NDUFB5^{helix-2}$ and ND2 to anchor this protein to the membrane arm (Figure 5C).

Lipid molecules also mediate the interactions of NDUFA11 with its partners. A cardiolipin molecule is in close proximity to $NDUFA11^{TMH1–2}$ and forms four hydrogen bonds with the side chains of $NDUFA11^{K44,\ R58,\ and\ Y59}$, while the aliphatic tails have a large number of hydrophobic interactions with ND4 and ND5 (Figures 5A and 5B). A PC molecule inserts into the crevice between the TMH of NDUFB4 and the N terminus of $NDUFA11^{TMH4}$. This PC molecule not only makes contacts with both proteins but also interacts with $ND5^{HL}$ through its aliphatic tail (Figure 5D). Interestingly, $NDUFA11^{W133}$ is close to a PE molecule, which has extensive interactions with the TMHs of ND2 and ND4 (Figure 5C). More interestingly, the tails of this PE molecule contact the tails of another PE molecule at opposite side, which is located between the hole of ND2, ND4, and $ND5^{HL}$ and forms more interactions with the proteins to further stabilize the complex (Figure 5A). The fact that lipid molecules can enhance the protein-protein interactions is consistent with the previous studies demonstrating that a large amount of different lipid bilayer components are present in the purified respiratory complexes (Pfeiffer et al., 2003; Sharpley et al., 2006; Shinzawa-Itoh et al., 2016). We therefore propose that the phospholipids play an important role for the assembly and possibly biological function of the SCs.

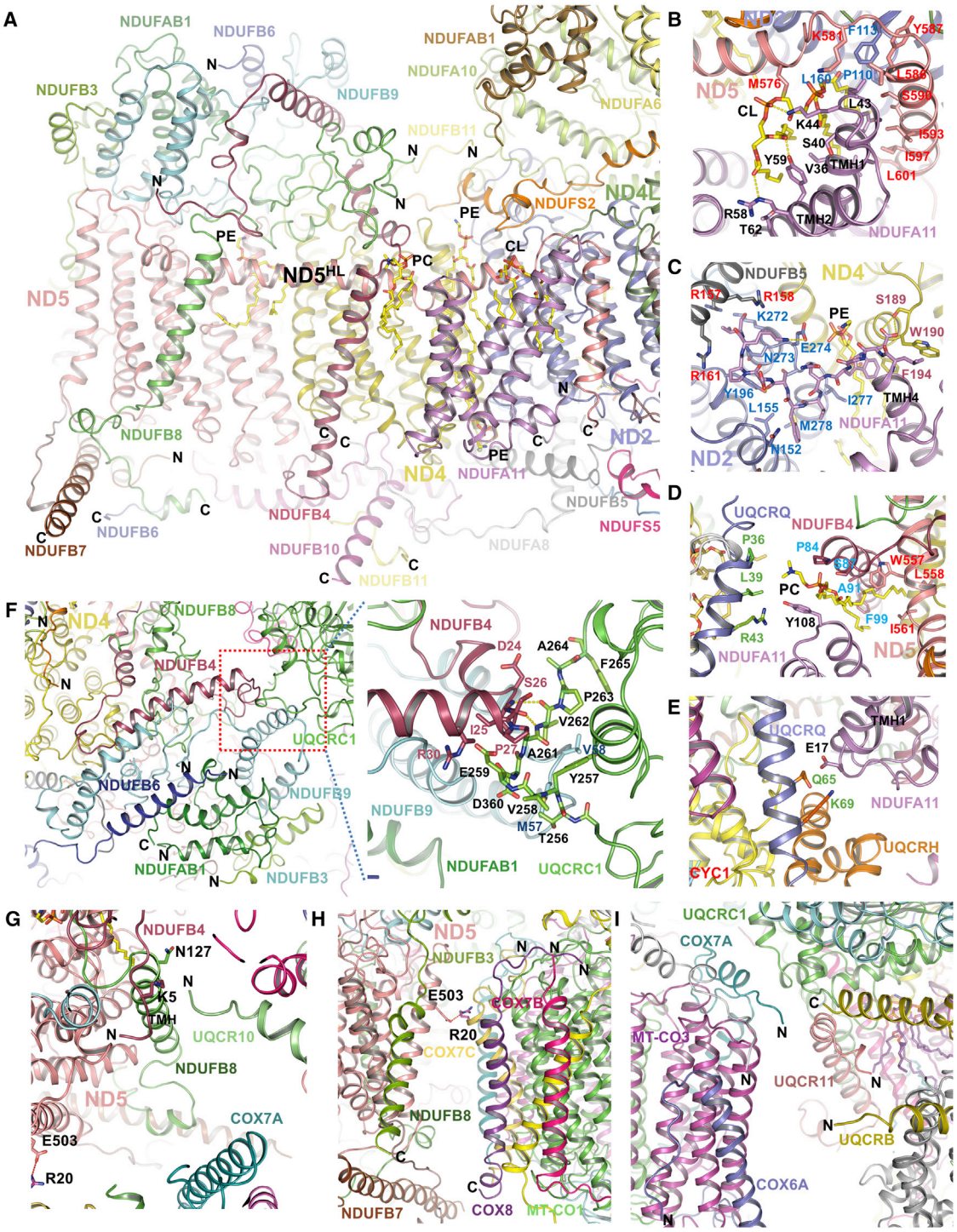

Figure 5. Interactions among CI, CIII, and CIV

(A) NDUFA11, NDUFB4, and NDUFB8 distribute in the middle of CI and CIII. Different subunits are colored individually and labeled with text in the same colors. The N and C termini of certain subunits are indicated. The phospholipid molecules are shown in yellow sticks and marked in black text.

(B) The interactions among NDUFA11, ND5, and the CL nearby. The yellow dashed lines represent hydrogen bonds. Residues of ND5 and NDUFA11 participating in the interactions are shown and labeled with red and black text, respectively. The CL molecule is shown as yellow sticks and marked.

(C) The C terminus of NDUFA11 contacts ND2, ND4, and NDUFB5. Figure is shown in the same way as (A).

(D) The PC molecule interacts with NDUFA11, NDUFB4, ND5, and UQCRQ. Residues participating in the hydrophobic interactions are shown and labeled in different colors. ND5, red; NDUFB4, blue; NDUFA11, black; UQCRQ, green. Others are shown in the same way as (A).

(legend continued on next page)

The other side of NDUFA11 faces the TM region of CIII, close to the UQCRB and UQCRQ subunits of one monomer of the CIII dimer (Figures 1C and 5E). These structural observations are consistent with previous studies showing that a mutation disrupting the first TM helix of NDUFA11 destabilized the entire complex (Berger et al., 2008) and that suppression of NDUFA11 expression disrupted the assembly of CI, resulting in the accumulation of 550- and 815-kDa CI sub-complexes and failure to form SCs (Andrews et al., 2013).

In addition to the central subunits descripted above, some distal subunits of the membrane arm contribute to the interaction between CI and CIII. The LYR-motif-containing supernumerary component NDUFB9 and an SDAP acyl-carrier protein, NDUFAB1, are located on the distal end of the membrane arm and on top of ND5 at the matrix side of CI. NDUFAB1, together with the N-terminal helix of NDUFB6, binds into the groove between the N-and C-lobes of NDUFB9 (Figure 5F). A highly conserved loop ($UQCRC1^{Y257\text{-}T266}$) of the UQCRC1 subunit on the matrix side inserts into the groove formed by $NDUFB9^{helix\text{-}3}$ and the N terminus of $NDUFB4^{helix\text{-}1}$ (Figure 5F). The LYR motif in the N-lobe of NDUFB9 is important for its binding to NDUFAB1 (Angerer et al., 2014) and could be crucial for stabilizing the CI-CIII interaction as well. This observation is consistent with the previous findings that mutations on NDUFB9 could cause CI deficiency (Haack et al., 2012), disturbance of the NAD^+/NADH balance, and promotion of tumor metastasis (Tan et al., 2014). Mutation of the NDUFB4 homolog gene *nuo-6* in *C. elegans* could lead to decreased ATP generation (Yang and Hekimi, 2010; Yee et al., 2014). When ATP usage is altered by stimulating mtROS signaling, this mutation could result in low oxygen consumption, slow growth, slow behavior, and increased lifespan.

CIV is adjacent to the concave surface formed by the CIII dimer and the distal end of the membrane arm of CI (Figure 1). Interestingly, both the N termini of NDUFB4 and the N termini of TMH of NDUFB8 are close to the N termini of UQCR10 of CIII. A short helix flowing the TMH of NDUFB8 is close to the COX7A subunit of CIV with a distance ~10 Å (Figure 5G). In addition to the hydrogen bond formed by the side chain of $ND5^{E503}$ and the side chain of $COX7C^{R20}$, the NDUFB3, NDUFB7, and NDUFB8 supernumerary subunits of CI are also close to COX7C and COX8 subunits of CIV (Figure 5H). At the other side, COX7A of CIV is close to the matrix side of UQCRC1, the N terminus of UQCR11, and the C terminus of UQCRB (Figure 5I). Interestingly, previous studies demonstrated that the longer isoform COX7A2L (containing 111 or 113 amino acids in different mouse strains) was only required for the CIII-CIV interaction (Cogliati et al., 2016; Ikeda et al., 2013; Lapuente-Brun et al., 2013; Mourier et al., 2014; Williams et al., 2016), while the short form was required for the formation of $SCI_1III_2IV_1$ instead of the COX7A2L as previously described (Lapuente-Brun et al., 2013).

The Phospholipid Molecules

Our structure clearly shows that a large amount of different lipid bilayer components, such as cardiolipin, PC, and PE, are involved in the protein-protein interactions (Figures 6 and S3). Previous studies suggested that hundreds of phospholipid molecules could bind to the respiratory supercomplexes to influence the enzymatic activities (Bavi et al., 2016; Dröse et al., 2002; Pfeiffer et al., 2003; Sharpley et al., 2006; Shinzawa-Itoh et al., 2016). Given the fact that we purified the endogenous complexes from porcine heart tissue with a mild detergent (digitonin), the lipids we found in the structure may be the physiologically relevant types and reflect actual binding positions in the complex in vivo. Interestingly, 7 of the 11 lipid molecules resolved in CI are involved in the interactions between core subunits, and the other 4 molecules participate in the interactions of the supernumerary subunits with the core subunits (Figure 6). Binding of phospholipids to the interfaces of the core subunits could well explain why the membrane arm organization is slightly different among different CI structures that have been solved in bacteria, yeast, or mammalian species, despite the fact that their sizes and structures are well conserved (Figures S6B and S6C). One explanation is that the detergents used in previous studies were strong enough to eliminate the lipids from the complex, and the other explanation could be that our structure is derived from $SCI_1III_2IV_1$, instead of a sub-complex. Nonetheless, the phospholipid molecules were clearly identified in all broken regions of the TMHs of ND1, ND2, ND4, and ND6, and those regions were shown to be important for proton translocation (Baradaran et al., 2013; Efremov and Sazanov, 2011; Zickermann et al., 2015) (Figure 6). The extensive interactions of the hydrophobic tails of phospholipids with those functionally critical regions indicate that the phospholipids might participate in the proton translocation processes as well. We hypothesize that by participating in protein-protein interactions, the phospholipids make the membrane arm more flexible. This flexibility enables the arm to change its conformation in response to electron transfer, effectively coupling electron transfer to proton translocation. Consistent with this hypothesis, previous studies have demonstrated that different phospholipids are required for the enzymatic activities of the purified complexes (Pfeiffer et al., 2003; Sharpley et al., 2006; Shinzawa-Itoh et al., 2016). Highly pure CI could regain enzymatic activity after incubation with a large amount of a mixture of PE, PC, and cardiolipin molecules (Dröse et al., 2002).

(E) The interactions between NDUFA11 and CIII. Figure is shown in the same way as (A).

(F) The UQCRC1 interacts with the NDUFB4 and NDUFB9 supernumerary subunits. The subunits are colored as labeled with text in the same colors, respectively. The N- and C-termini of some certain subunits are indicated. The interaction residues are shown as sticks and indicated. The yellow dashed lines represent hydrogen bonds.

(G) NDUFB8 mediates the interactions between CI with both CIII and CIV.

(H) Interactions between CIV and CI. The subunits participating in the interactions are colored individually and labeled with text in the same colors. The N and C termini are indicated. The yellow dashed lines represent hydrogen bonds.

(I) Interactions between CIV and CIII. The subunits distributing in the interface of CIV and CIII are shown and marked. The N and C termini are indicated.

See also Figures S5 and S7.

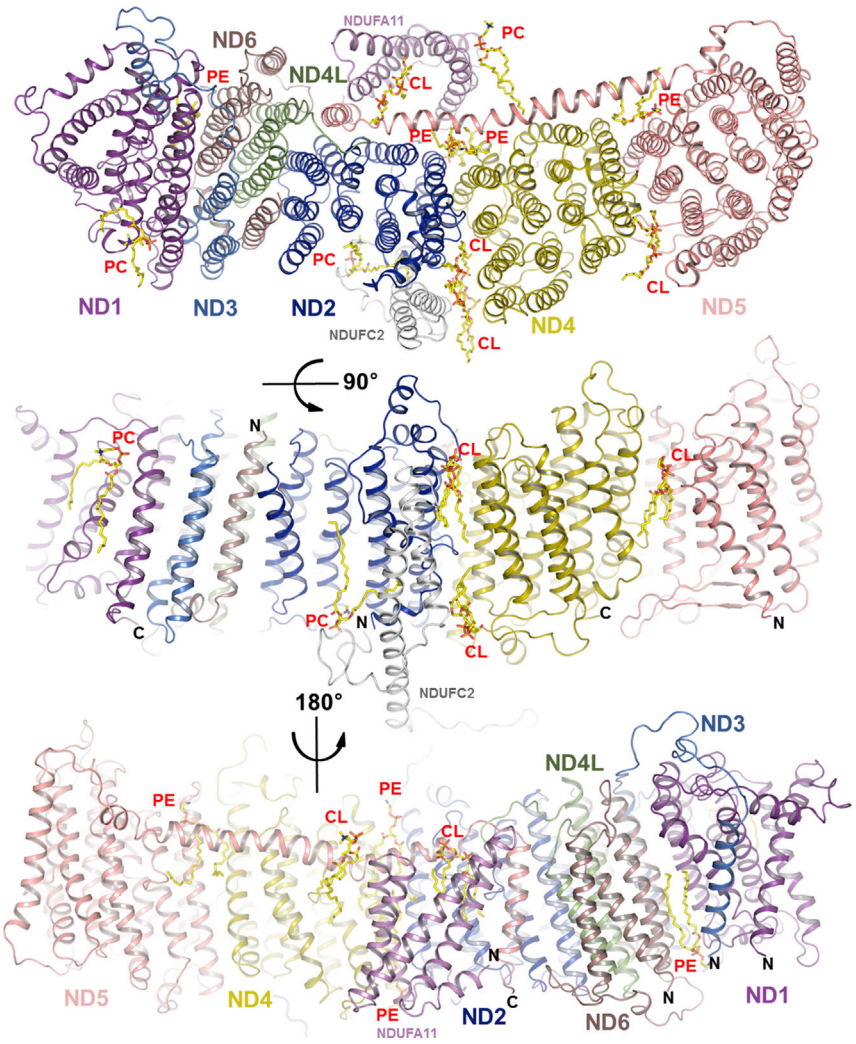

Figure 6. Phospholipids Participate in Protein-Protein Interactions

Cartoon representation of part of the membrane arm structure in three different rotations. The top panel view is from the matrix side. Phospholipids are shown as yellow sticks. All the broken regions of the discontinued TMHs in ND1, ND2, ND4, and ND6 are close to at least one carbonic tail of the phospholipid molecules.

See also Figure S3.

DISCUSSION

The structure and function of respiratory complexes have been intensively investigated over the past few decades (Baradaran et al., 2013; Berrisford et al., 2016; Efremov et al., 2010; Efremov and Sazanov, 2011; Feng et al., 2012; Fiedorczuk et al., 2016; Gu et al., 2016; Guo et al., 2016; Hunte et al., 2010; Iwata et al., 1998; Letts et al., 2016; Sazanov and Hinchliffe, 2006; Tsukihara et al., 1995, 1996; Vinothkumar et al., 2014; Zhang et al., 1998; Zhu et al., 2016; Zickermann et al., 2015). However, there has been a lack of high-resolution structures of mammalian complexes, with 5.4- and 5.8-Å-resolution cryo-EM architectures of $SCI_1III_2IV_1$ resolved very recently (Gu et al., 2016; Letts et al., 2016). In the present study, we purified the predominant form of the supercomplex ($I_1III_2IV_1$) from porcine heart and obtained a near-atomic-resolution structure using single-particle cryo-EM. Using a segmentation refinement method, we obtained the 3.6-Å-resolution map of CI and assigned 44 subunits into the structure (Figure 2), with the vast majority of subunits containing side chain information (Table S1). The overall structure reveals that the 30 supernumerary subunits form a sandal-like cage to hold the 14 core subunits (Figure 2). CI is traditionally divided into four functional modules, but our structural study shows that the core and accessory subunits can cross the boundary and make interactions between modules. For example, the N terminus of the M_P module core subunit NDUFS2 extends to P_P and P_D modules and end at ND4 (Figures 2B, 3A, 3B, and S6D). Among the 44 subunits, NDUFA8, NDUFA13, NDUFS4, NDUFS8, NDUFB10, NDUFB9, NDUFB5, ND5, and NDUFS2 form extensive interactions with 9, 9, 10, 10, 11, 13, 15, 16, and 17 other subunits, respectively. These proteins interact with each other directly or indirectly to stabilize the entire complex (Figures 2, 3, and S6D). These structural observations indicate that CI acts as an integral unit to perform the enzymatic activity. Many subunits break the module boundaries and cannot be precisely assigned to a particular module.

Previous electron tomography and freeze-fracture EM studies indicated that the respiratory complexes could form high-order assemblies of respiratory rows or strings (Allen et al., 1989; Davies et al., 2011; Nicastro et al., 2000). Indeed, we and others detected high-molecular-weight bands above $SCI_1III_2IV_1$ (Figures S7A and S7B) (Althoff et al., 2011; Dudkina et al., 2011; Schäfer et al., 2006; Stroh et al., 2004), suggesting that the respiratory complexes could exist in higher oligomeric states. Given the fact that CIII forms a symmetric homodimer, binding of an additional CI to the other side of the dimeric CIII through its supernumerary components, such as NDUFA11 and NDUFB9, could lead to the formation of a circular supra-supercomplex $SCI_2III_2IV_2$ (Figures S7C and S7D). In this model, the two-fold axis is centered at the CIII homodimer. Based on the calculated distance, the reduced Cyt.*c* could efficiently diffuse to both CIVs (Figure S7D), thereby increasing the electron transfer efficiency and precluding the production of ROS. In fact, we have detected a minor population of particles with an arrangement consistent with the circular model (Figures S7E and S7F). In addition, a previous single-particle EM study suggested the presence of SCI_2III_2 in potato (Bultema et al., 2009), which has

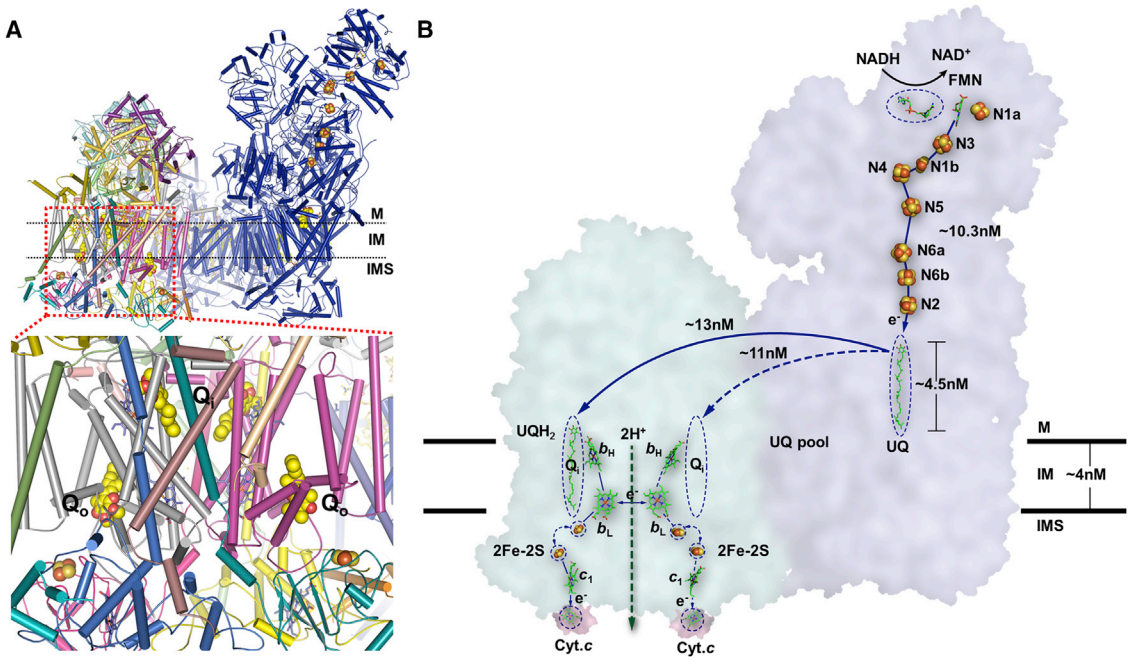

Figure 7. Electron Transfer Pathway in CI and CIII

(A) Structural assignment of electron carriers in CI and CIII. The bottom panel shows a detailed arrangement of Q_i and Q_o sites reported in previous studies. The UQ2s shown in spheres are modeled into a Q-chamber in CI and the hypothetical Q_o and Q_i binding sites in CIII. The heme molecules are shown in sticks, and the Fe-S clusters are shown in spheres. The image is viewed along the membrane. M, matrix; IM, inner membrane; IMS, intermembrane space.

(B) Electron transfer and coupled H^+ transport mechanism. Electron trail from NADH in CI to Cyt.*c* in CIII is shown in blue solid line. An alternative electron trail is shown as a blue dashed line. Elements in the blue dashed circle are movable electron carriers. The transport of H^+ is shown as a green dashed line. The thickness of mitochondrial inner membrane and the length of UQ are shown. The length of the electron trail from FMN to N2 in CI is ~10.3 nm. The distance from the UQ-binding pocket in CI to the Q_i site in the distal CIII monomer is ~13 nm, while the distance to the Q_i site in the proximal CIII monomer is ~11 nm. Distances are measured from our structure. The hemes and UQ molecules are shown as sticks, and the FeS clusters are shown as spheres.

an architecture similar to our circular model. How the respiratory strings are formed by CI, CIII, and CIV in situ on the inner mitochondrial membrane requires further investigations using a non-invasive method.

An unoccupied space is observed between the matrix regions of CI and CIII (Figures 1 and 7A). This opening might be the UQ (UQ10) tunnel that allows diffusion of UQH_2 from CI to CIII. Previous studies suggested that there were two UQ-binding sites in each CIII monomer (Gao et al., 2003), including the Q_o site, which was proposed to oxidize UQH_2 to UQ by heme c_1, and the Q_i site, which was near the matrix side and responsible for the reduction of UQ to UQH_2 by heme b_H (Figure 7A). The proposed electron transfer processes are known as the Q-cycle model (Mitchell, 1975a, 1975b; Pietras et al., 2016). In this model, the two types of ubiquinone-binding sites face opposite sides of the membrane: one site oxidizes ubiquinol (Q_o), whereas the other reduces ubiquinone (Q_i). Although the Q-cycle model has been proposed for ~40 years (Mitchell, 1975a, 1975b), the structure with the Q_i site occupied by native UQ is still missing (Gao et al., 2003). Furthermore, there are no reliable data to support the claim that the Q_o site is a functional UQH_2-binding site (Pietras et al., 2016). It is difficult to envision how the UQH_2 released from CI with its hydrophilic head group at the matrix side can insert into the IMS-facing Q_o site with the head group flipping over in the membrane (Figure 7A). More puzzlingly, if UQ could be reduced to UQH_2 at the Q_i site, it would easily diffuse to the membrane with the head group at the matrix side, causing accumulation of UQH_2 around the UQ-tunnel in CI and resulting in reduced efficiency of the respiratory system. Here, based on our structural observation, we propose a mechanism that could better explain how electron transfer is coupled to proton translocation in CIII. The distances between the UQ binding site in CI and the two Q_i sites in the CIII dimer are ~110 and 130 Å, respectively. Structural analysis indicates that the UQH_2 diffused from CI could access the Q_i site in the distal CIII monomer more easily than the Q_i site in the proximal CIII monomer. This structural observation favors a different mechanism to couple electron transfer from UQH_2 to Cyt.*c* with proton translocation in CIII.

In our model (Figure 7B), the UQH_2 is released from CI, diffuses to the Q_i site close to the heme b_H of CIII, transfers one electron to heme b_H, and changes to a semiQ (SQ) radical. Then, the heme b_H transfers the electron to heme b_L and simultaneously accepts another electron from the SQ radical. The oxidized UQ is released from the Q_i site. After the heme b_L obtains one electron, it transfers the electron either to the heme b_L in the other CIII monomer or causes a conformational change

of the ISP subunit in the same CIII monomer from the "*int*" state to the "*b*" state to move its [2Fe-2S] cluster closer to the heme b_L. In the former possibility, after the electron is transferred to another heme b_L, the first heme b_L can accept another electron from heme b_H (Figure 7B). We favor this possibility for two reasons. First, one UQH_2 can readily distribute two electrons to two heme b_Ls, limiting the lifetime of the SQ radical to minimize the generation of ROS. Second, as previous studies demonstrated, transferring the electrons between the two neighboring heme b_L molecules could be much faster than the conformational change of ISP proteins (Swierczek et al., 2010), in which CIII needs to wait for the binding of the diffusible substrate Cyt.*c*. Thus, we propose that the electron transfer between heme b_Ls occurs prior to the conformational change of ISP proteins.

After both heme b_Ls acquire an electron and the ISP proteins change to the "*b*" state, the electrons could be transferred to the two [2Fe-2S] clusters, and then the ISP proteins change to the "c_1" state to transfer the electrons to the heme c_1 from their [2Fe-2S] clusters. Finally, each heme c_1 transfers a single electron to Cyt.*c*. Together with the transfer of electrons, the two protons dissociated from the UQH_2 might be translocated from the Q_i site to the IMS using the redox energy released by electron transfer. In conclusion, in each cycle of electron transfer cascade, one molecule of UQH_2 distributes two electrons to two separate Cyt.*c* electron acceptors, and at the same time, CIII translocates two protons from UQH_2 to IMS (Figure 7B). Further investigations will be needed to test this model. All in all, the electron transfer coupling proton translocation reaction in CIII could be indicated as: 2Cyt.*c* (oxidized) + QH_2 → 2Cyt.*c* (reduced) + Q + $2H^+$ (IMS).

Conclusions

Although the biological functions and structures of respiratory complexes have been extensively studied, the mechanism underlying the coupling of electron transfer and proton translocation remains elusive. In the present study, we solved a 4.0-Å-resolution structure of $SCI_1III_2IV_1$, with SCI_1III_2 reaching near-atomic resolution (Figures 1 and S1). The structure reveals that the 14 core subunits of CI together with 30 accessory subunits form an integral unit to transfer two electrons from NADH to UQ. Four accessory subunits (NDUFA11, NDUFB4, NDUFB8, and NDUFB9) of CI mainly contribute to interactions with the CIII dimer through direct protein-protein interactions or through phospholipid molecules in the CI-CIII groove (Figure 5). The previous Q-cycle model posits that UQ and UQH_2 can bind to Q_i and Q_o sites, respectively, and only one electron of UQH_2 can be delivered to Cyt.*c* in one cycle (Mitchell, 1975a, 1975b; Pietras et al., 2016). Our structure is more consistent with an alternative model, in which the UQH_2 diffused from CI can only bind to the Q_i sites in the CIII dimer and can deliver two electrons to two Cyt.*c* proteins at one time (Figure 7B). Collectively, the structural information reported in our study establishes the organizing principles of the respiration supercomplexes, reveals protein-protein and protein-cofactor binding interactions with exquisite details, suggests an alternative testable model for electron transfer, and paves the road for future in-depth understanding of the OXPHOS system as a whole.

STAR★METHODS

Detailed methods are provided in the online version of this paper and include the following:

- KEY RESOURCES TABLE
- CONTACT FOR REAGENT AND RESOURCE SHARING
- EXPERIMENTAL MODEL AND SUBJECT DETAILS
  - Animals
- METHOD DETAILS
  - Isolation of Mitochondria from Porcine Heart
  - Respiratory Supercomplex $I_1III_2IV_1$ Purification
  - Blue Native PAGE
  - NBT Staining
  - Cryo-EM Data Acquisition and Processing
  - Image Processing
  - Model Building and Refinement
- QUANTIFICATION AND STATISTICAL ANALYSIS
- DATA AND SOFTWARE AVAILABILITY

SUPPLEMENTAL INFORMATION

Supplemental Information includes seven figures and one table and can be found with this article online at http://dx.doi.org/10.1016/j.cell.2016.11.012.

AUTHOR CONTRIBUTIONS

M.Y. conceived, designed, and supervised the project, built the model, and wrote the manuscript. J.G. and R.G. did the protein purification and detergent screening. M.W. and Y.H. performed EM sample preparation, data collection, and structural determination. All authors discussed the data reported in this paper.

ACKNOWLEDGMENTS

We would like to thank Dr. Mengqiu Dong and Dan Tan (National Institute of Biological Sciences, Beijing) for the mass spectrometry analyses, Dr. Jianlin Lei for cryo-EM data collection, and the Tsinghua University Branch of China National Center for Protein Sciences (Beijing) for providing the facility support. This work was supported by grants from the Ministry of Science and Technology of China (2016YFA0501100 and 2012CB911101), the National Science Fund for Distinguished Young Scholars (31625008), and the National Natural Science Foundation of China (31030020 and 31170679).

Received: September 30, 2016
Revised: October 27, 2016
Accepted: November 3, 2016
Published: December 1, 2016

REFERENCES

Acín-Pérez, R., Bayona-Bafaluy, M.P., Fernández-Silva, P., Moreno-Loshuertos, R., Pérez-Martos, A., Bruno, C., Moraes, C.T., and Enríquez, J.A. (2004). Respiratory complex III is required to maintain complex I in mammalian mitochondria. Mol. Cell *13*, 805–815.

Acín-Pérez, R., Fernández-Silva, P., Peleato, M.L., Pérez-Martos, A., and Enriquez, J.A. (2008). Respiratory active mitochondrial supercomplexes. Mol. Cell *32*, 529–539.

Adams, P.D., Grosse-Kunstleve, R.W., Hung, L.W., Ioerger, T.R., McCoy, A.J., Moriarty, N.W., Read, R.J., Sacchettini, J.C., Sauter, N.K., and Terwilliger, T.C. (2002). PHENIX: building new software for automated crystallographic structure determination. Acta Crystallogr. D Biol. Crystallogr. *58*, 1948–1954.

Adams, P.D., Afonine, P.V., Bunkóczi, G., Chen, V.B., Davis, I.W., Echols, N., Headd, J.J., Hung, L.W., Kapral, G.J., Grosse-Kunstleve, R.W., et al. (2010). PHENIX: a comprehensive Python-based system for macromolecular structure solution. Acta Crystallogr. D Biol. Crystallogr. *66*, 213–221.

Allen, R.D., Schroeder, C.C., and Fok, A.K. (1989). An investigation of mitochondrial inner membranes by rapid-freeze deep-etch techniques. J. Cell Biol. *108*, 2233–2240.

Althoff, T., Mills, D.J., Popot, J.L., and Kühlbrandt, W. (2011). Arrangement of electron transport chain components in bovine mitochondrial supercomplex I1III2IV1. EMBO J. *30*, 4652–4664.

Andrews, B., Carroll, J., Ding, S., Fearnley, I.M., and Walker, J.E. (2013). Assembly factors for the membrane arm of human complex I. Proc. Natl. Acad. Sci. USA *110*, 18934–18939.

Angerer, H., Radermacher, M., Mańkowska, M., Steger, M., Zwicker, K., Heide, H., Wittig, I., Brandt, U., and Zickermann, V. (2014). The LYR protein subunit NB4M/NDUFA6 of mitochondrial complex I anchors an acyl carrier protein and is essential for catalytic activity. Proc. Natl. Acad. Sci. USA *111*, 5207–5212.

Baradaran, R., Berrisford, J.M., Minhas, G.S., and Sazanov, L.A. (2013). Crystal structure of the entire respiratory complex I. Nature *494*, 443–448.

Bavi, N., Cortes, D.M., Cox, C.D., Rohde, P.R., Liu, W., Deitmer, J.W., Bavi, O., Strop, P., Hill, A.P., Rees, D., et al. (2016). The role of MscL amphipathic N terminus indicates a blueprint for bilayer-mediated gating of mechanosensitive channels. Nat. Commun. *7*, 11984.

Belevich, I., Bloch, D.A., Belevich, N., Wikström, M., and Verkhovsky, M.I. (2007). Exploring the proton pump mechanism of cytochrome c oxidase in real time. Proc. Natl. Acad. Sci. USA *104*, 2685–2690.

Benard, G., Faustin, B., Galinier, A., Rocher, C., Bellance, N., Smolkova, K., Casteilla, L., Rossignol, R., and Letellier, T. (2008). Functional dynamic compartmentalization of respiratory chain intermediate substrates: implications for the control of energy production and mitochondrial diseases. Int. J. Biochem. Cell Biol. *40*, 1543–1554.

Berger, I., Hershkovitz, E., Shaag, A., Edvardson, S., Saada, A., and Elpeleg, O. (2008). Mitochondrial complex I deficiency caused by a deleterious NDUFA11 mutation. Ann. Neurol. *63*, 405–408.

Berrisford, J.M., Baradaran, R., and Sazanov, L.A. (2016). Structure of bacterial respiratory complex I. Biochim. Biophys. Acta *1857*, 892–901.

Blaza, J.N., Serreli, R., Jones, A.J., Mohammed, K., and Hirst, J. (2014). Kinetic evidence against partitioning of the ubiquinone pool and the catalytic relevance of respiratory-chain supercomplexes. Proc. Natl. Acad. Sci. USA *111*, 15735–15740.

Brandt, U. (2006). Energy converting NADH:quinone oxidoreductase (complex I). Annu. Rev. Biochem. *75*, 69–92.

Bultema, J.B., Braun, H.P., Boekema, E.J., and Kouril, R. (2009). Megacomplex organization of the oxidative phosphorylation system by structural analysis of respiratory supercomplexes from potato. Biochim. Biophys. Acta *1787*, 60–67.

Chacinska, A., Koehler, C.M., Milenkovic, D., Lithgow, T., and Pfanner, N. (2009). Importing mitochondrial proteins: machineries and mechanisms. Cell *138*, 628–644.

Chen, S., McMullan, G., Faruqi, A.R., Murshudov, G.N., Short, J.M., Scheres, S.H., and Henderson, R. (2013). High-resolution noise substitution to measure overfitting and validate resolution in 3D structure determination by single particle electron cryomicroscopy. Ultramicroscopy *135*, 24–35.

Cogliati, S., Calvo, E., Loureiro, M., Guaras, A.M., Nieto-Arellano, R., Garcia-Poyatos, C., Ezkurdia, I., Mercader, N., Vazquez, J., and Enriquez, J.A. (2016). Mechanism of super-assembly of respiratory complexes III and IV. Nature. Published online October 24, 2016. http://dx.doi.org/10.1038/nature20157.

Davies, K.M., Strauss, M., Daum, B., Kief, J.H., Osiewacz, H.D., Rycovska, A., Zickermann, V., and Kühlbrandt, W. (2011). Macromolecular organization of ATP synthase and complex I in whole mitochondria. Proc. Natl. Acad. Sci. USA *108*, 14121–14126.

Dröse, S., Zwicker, K., and Brandt, U. (2002). Full recovery of the NADH: ubiquinone activity of complex I (NADH:ubiquinone oxidoreductase) from Yarrowia lipolytica by the addition of phospholipids. Biochim. Biophys. Acta *1556*, 65–72.

Dudkina, N.V., Kudryashev, M., Stahlberg, H., and Boekema, E.J. (2011). Interaction of complexes I, III, and IV within the bovine respirasome by single particle cryoelectron tomography. Proc. Natl. Acad. Sci. USA *108*, 15196–15200.

Efremov, R.G., and Sazanov, L.A. (2011). Structure of the membrane domain of respiratory complex I. Nature *476*, 414–420.

Efremov, R.G., Baradaran, R., and Sazanov, L.A. (2010). The architecture of respiratory complex I. Nature *465*, 441–445.

Emsley, P., and Cowtan, K. (2004). Coot: model-building tools for molecular graphics. Acta Crystallogr. D Biol. Crystallogr. *60*, 2126–2132.

Emsley, P., Lohkamp, B., Scott, W.G., and Cowtan, K. (2010). Features and development of Coot. Acta Crystallogr. D Biol. Crystallogr. *66*, 486–501.

Enríquez, J.A. (2016). Supramolecular organization of respiratory complexes. Annu. Rev. Physiol. *78*, 533–561.

Feng, Y., Li, W., Li, J., Wang, J., Ge, J., Xu, D., Liu, Y., Wu, K., Zeng, Q., Wu, J.W., et al. (2012). Structural insight into the type-II mitochondrial NADH dehydrogenases. Nature *491*, 478–482.

Fiedorczuk, K., Letts, J.A., Degliesposti, G., Kaszuba, K., Skehel, M., and Sazanov, L.A. (2016). Atomic structure of the entire mammalian mitochondrial complex I. Nature *538*, 406–410.

Gao, X., Wen, X., Esser, L., Quinn, B., Yu, L., Yu, C.A., and Xia, D. (2003). Structural basis for the quinone reduction in the bc1 complex: a comparative analysis of crystal structures of mitochondrial cytochrome bc1 with bound substrate and inhibitors at the Qi site. Biochemistry *42*, 9067–9080.

Genova, M.L. (2014). Electron transport in the mitochondrial respiratory chain. In The Structural Basis of Biological Energy Generation, M.F. Hohmann-Marriott, ed. (Springer), pp. 401–417.

Gu, J., Wu, M., Guo, R., Yan, K., Lei, J., Gao, N., and Yang, M. (2016). The architecture of the mammalian respirasome. Nature *537*, 639–643.

Guo, R., Gu, J., Wu, M., and Yang, M. (2016). Amazing structure of respirasome: unveiling the secrets of cell respiration. Protein Cell. Published online October 14, 2016. http://dx.doi.org/10.1007/s13238-016-0329-7.

Haack, T.B., Madignier, F., Herzer, M., Lamantea, E., Danhauser, K., Invernizzi, F., Koch, J., Freitag, M., Drost, R., Hillier, I., et al. (2012). Mutation screening of 75 candidate genes in 152 complex I deficiency cases identifies pathogenic variants in 16 genes including NDUFB9. J. Med. Genet. *49*, 83–89.

Hirst, J. (2013). Mitochondrial complex I. Annu. Rev. Biochem. *82*, 551–575.

Hunte, C., Zickermann, V., and Brandt, U. (2010). Functional modules and structural basis of conformational coupling in mitochondrial complex I. Science *329*, 448–451.

Ikeda, K., Shiba, S., Horie-Inoue, K., Shimokata, K., and Inoue, S. (2013). A stabilizing factor for mitochondrial respiratory supercomplex assembly regulates energy metabolism in muscle. Nat. Commun. *4*, 2147.

Iwata, S., Lee, J.W., Okada, K., Lee, J.K., Iwata, M., Rasmussen, B., Link, T.A., Ramaswamy, S., and Jap, B.K. (1998). Complete structure of the 11-subunit bovine mitochondrial cytochrome bc1 complex. Science *281*, 64–71.

Kucukelbir, A., Sigworth, F.J., and Tagare, H.D. (2014). Quantifying the local resolution of cryo-EM density maps. Nat. Methods *11*, 63–65.

Kuonen, D.R., Roberts, P.J., and Cottingham, I.R. (1986). Purification and analysis of mitochondrial membrane proteins on nondenaturing gradient polyacrylamide gels. Anal. Biochem. *153*, 221–226.

Lamantea, E., Carrara, F., Mariotti, C., Morandi, L., Tiranti, V., and Zeviani, M. (2002). A novel nonsense mutation (Q352X) in the mitochondrial cytochrome b gene associated with a combined deficiency of complexes I and III. Neuromuscul. Disord. *12*, 49–52.

Lapuente-Brun, E., Moreno-Loshuertos, R., Acín-Pérez, R., Latorre-Pellicer, A., Colás, C., Balsa, E., Perales-Clemente, E., Quirós, P.M., Calvo, E., Rodríguez-Hernández, M.A., et al. (2013). Supercomplex assembly determines

electron flux in the mitochondrial electron transport chain. Science *340*, 1567–1570.

Letts, J.A., Fiedorczuk, K., and Sazanov, L.A. (2016). The architecture of respiratory supercomplexes. Nature *537*, 644–648.

Li, X., Mooney, P., Zheng, S., Booth, C.R., Braunfeld, M.B., Gubbens, S., Agard, D.A., and Cheng, Y. (2013). Electron counting and beam-induced motion correction enable near-atomic-resolution single-particle cryo-EM. Nat. Methods *10*, 584–590.

Maranzana, E., Barbero, G., Falasca, A.I., Lenaz, G., and Genova, M.L. (2013). Mitochondrial respiratory supercomplex association limits production of reactive oxygen species from complex I. Antioxid. Redox Signal. *19*, 1469–1480.

Mindell, J.A., and Grigorieff, N. (2003). Accurate determination of local defocus and specimen tilt in electron microscopy. J. Struct. Biol. *142*, 334–347.

Mitchell, P. (1961). Coupling of phosphorylation to electron and hydrogen transfer by a chemi-osmotic type of mechanism. Nature *191*, 144–148.

Mitchell, P. (1975a). The protonmotive Q cycle: a general formulation. FEBS Lett. *59*, 137–139.

Mitchell, P. (1975b). Protonmotive redox mechanism of the cytochrome b-c1 complex in the respiratory chain: protonmotive ubiquinone cycle. FEBS Lett. *56*, 1–6.

Moreno-Lastres, D., Fontanesi, F., García-Consuegra, I., Martín, M.A., Arenas, J., Barrientos, A., and Ugalde, C. (2012). Mitochondrial complex I plays an essential role in human respirasome assembly. Cell Metab. *15*, 324–335.

Moriarty, N.W., Grosse-Kunstleve, R.W., and Adams, P.D. (2009). electronic Ligand Builder and Optimization Workbench (eLBOW): a tool for ligand coordinate and restraint generation. Acta Crystallogr. D Biol. Crystallogr. *65*, 1074–1080.

Mourier, A., Matic, S., Ruzzenente, B., Larsson, N.G., and Milenkovic, D. (2014). The respiratory chain supercomplex organization is independent of COX7a2l isoforms. Cell Metab. *20*, 1069–1075.

Nicastro, D., Frangakis, A.S., Typke, D., and Baumeister, W. (2000). Cryo-electron tomography of neurospora mitochondria. J. Struct. Biol. *129*, 48–56.

Pettersen, E.F., Goddard, T.D., Huang, C.C., Couch, G.S., Greenblatt, D.M., Meng, E.C., and Ferrin, T.E. (2004). UCSF Chimera–a visualization system for exploratory research and analysis. J. Comput. Chem. *25*, 1605–1612.

Pfeiffer, K., Gohil, V., Stuart, R.A., Hunte, C., Brandt, U., Greenberg, M.L., and Schägger, H. (2003). Cardiolipin stabilizes respiratory chain supercomplexes. J. Biol. Chem. *278*, 52873–52880.

Pietras, R., Sarewicz, M., and Osyczka, A. (2016). Distinct properties of semiquinone species detected at the ubiquinol oxidation Qo site of cytochrome bc1 and their mechanistic implications. J. R. Soc. Interface *13*, 20160133.

Sazanov, L.A. (2015). A giant molecular proton pump: structure and mechanism of respiratory complex I. Nat. Rev. Mol. Cell Biol. *16*, 375–388.

Sazanov, L.A., and Hinchliffe, P. (2006). Structure of the hydrophilic domain of respiratory complex I from Thermus thermophilus. Science *311*, 1430–1436.

Schäfer, E., Seelert, H., Reifschneider, N.H., Krause, F., Dencher, N.A., and Vonck, J. (2006). Architecture of active mammalian respiratory chain supercomplexes. J. Biol. Chem. *281*, 15370–15375.

Schäfer, E., Dencher, N.A., Vonck, J., and Parcej, D.N. (2007). Three-dimensional structure of the respiratory chain supercomplex I1III2IV1 from bovine heart mitochondria. Biochemistry *46*, 12579–12585.

Schägger, H., and Pfeiffer, K. (2000). Supercomplexes in the respiratory chains of yeast and mammalian mitochondria. EMBO J. *19*, 1777–1783.

Scheres, S.H. (2012). RELION: implementation of a Bayesian approach to cryo-EM structure determination. J. Struct. Biol. *180*, 519–530.

Scheres, S.H., and Chen, S. (2012). Prevention of overfitting in cryo-EM structure determination. Nat. Methods *9*, 853–854.

Schmidt, O., Pfanner, N., and Meisinger, C. (2010). Mitochondrial protein import: from proteomics to functional mechanisms. Nat. Rev. Mol. Cell Biol. *11*, 655–667.

Sharpley, M.S., Shannon, R.J., Draghi, F., and Hirst, J. (2006). Interactions between phospholipids and NADH:ubiquinone oxidoreductase (complex I) from bovine mitochondria. Biochemistry *45*, 241–248.

Shinzawa-Itoh, K., Shimomura, H., Yanagisawa, S., Shimada, S., Takahashi, R., Oosaki, M., Ogura, T., and Tsukihara, T. (2016). Purification of active respiratory supercomplex from bovine heart mitochondria enables functional studies. J. Biol. Chem. *291*, 4178–4184.

Smirnov, A.Y., and Nori, F. (2012). Modeling the Q-cycle mechanism of transmembrane energy conversion. Phys. Biol. *9*, 016011.

Stroh, A., Anderka, O., Pfeiffer, K., Yagi, T., Finel, M., Ludwig, B., and Schägger, H. (2004). Assembly of respiratory complexes I, III, and IV into NADH oxidase supercomplex stabilizes complex I in Paracoccus denitrificans. J. Biol. Chem. *279*, 5000–5007.

Swierczek, M., Cieluch, E., Sarewicz, M., Borek, A., Moser, C.C., Dutton, P.L., and Osyczka, A. (2010). An electronic bus bar lies in the core of cytochrome bc1. Science *329*, 451–454.

Tan, A.S., Baty, J.W., and Berridge, M.V. (2014). The role of mitochondrial electron transport in tumorigenesis and metastasis. Biochim. Biophys. Acta *1840*, 1454–1463.

Tang, G., Peng, L., Baldwin, P.R., Mann, D.S., Jiang, W., Rees, I., and Ludtke, S.J. (2007). EMAN2: an extensible image processing suite for electron microscopy. J. Struct. Biol. *157*, 38–46.

Tsukihara, T., Aoyama, H., Yamashita, E., Tomizaki, T., Yamaguchi, H., Shinzawa-Itoh, K., Nakashima, R., Yaono, R., and Yoshikawa, S. (1995). Structures of metal sites of oxidized bovine heart cytochrome c oxidase at 2.8 A. Science *269*, 1069–1074.

Tsukihara, T., Aoyama, H., Yamashita, E., Tomizaki, T., Yamaguchi, H., Shinzawa-Itoh, K., Nakashima, R., Yaono, R., and Yoshikawa, S. (1996). The whole structure of the 13-subunit oxidized cytochrome c oxidase at 2.8 A. Science *272*, 1136–1144.

Vinothkumar, K.R., Zhu, J., and Hirst, J. (2014). Architecture of mammalian respiratory complex I. Nature *515*, 80–84.

Williams, E.G., Wu, Y., Jha, P., Dubuis, S., Blattmann, P., Argmann, C.A., Houten, S.M., Amariuta, T., Wolski, W., Zamboni, N., et al. (2016). Systems proteomics of liver mitochondria function. Science *352*, aad0189.

Wittig, I., Braun, H.P., and Schägger, H. (2006). Blue native PAGE. Nat. Protoc. *1*, 418–428.

Yang, W., and Hekimi, S. (2010). Two modes of mitochondrial dysfunction lead independently to lifespan extension in Caenorhabditis elegans. Aging Cell *9*, 433–447.

Yee, C., Yang, W., and Hekimi, S. (2014). The intrinsic apoptosis pathway mediates the pro-longevity response to mitochondrial ROS in C. elegans. Cell *157*, 897–909.

Zhang, Z., Huang, L., Shulmeister, V.M., Chi, Y.I., Kim, K.K., Hung, L.W., Crofts, A.R., Berry, E.A., and Kim, S.H. (1998). Electron transfer by domain movement in cytochrome bc1. Nature *392*, 677–684.

Zhu, J., Vinothkumar, K.R., and Hirst, J. (2016). Structure of mammalian respiratory complex I. Nature *536*, 354–358.

Zickermann, V., Wirth, C., Nasiri, H., Siegmund, K., Schwalbe, H., Hunte, C., and Brandt, U. (2015). Structural biology. Mechanistic insight from the crystal structure of mitochondrial complex I. Science *347*, 44–49.

STAR★METHODS

KEY RESOURCES TABLE

REAGENT or RESOURCE	SOURCE	IDENTIFIER
Biological Samples		
Healthy porcine heart tissue	Bought from slaughterhouse of Tsinghua University campus	N/A
Chemicals, Peptides, and Recombinant Proteins		
Trizma base	Sigma	T4661; CAS: 77-86-1
D-Sorbitol	Sigma	S1876; CAS: 50-70-4
KCl	Sigma-Aldrich	746436; CAS: 7447-40-7
EGTA	Sigma-Aldrich	E4378; CAS: 67-42-5
BSA	AMRESCO	0332; CAS: 9048-46-8
Percoll	GE Healthcare	17-0891-09
Digitonin	Sigma	D141; CAS: 11024-24-1
Glycine	Sigma	G7126; CAS: 56-40-6
4-Nitro blue tetrazolium chloride (NBT)	Sigma-Aldrich	N6876; CAS: 298-83-9
β-Nicotinamide adenine dinucleotide, reduced (β-NADH)	Sigma	N8129; CAS: 606-68-8 (Anhydrous)
6-Aminohexanoic acid	Sigma-Aldrich	07260; CAS: 60-32-2
Coomassie brilliant blue G-250	AMRESCO	0615; CAS: 6104-58-1
Glycerol	Sigma-Aldrich	G6279; CAS: 56-81-5
Ponceau S	Sigma-Aldrich	P3504; CAS: 6226-79-5
Acrylamide	Vetec	V900845; CAS: 79-06-1
N,N′-Methylenebis(acrylamide)	Vetec	V900301; CAS: 110-26-9
Tricine	Sigma	T0377; CAS: 5704-04-1
Imidazole	Aldrich	I202; CAS: 288-32-4
Ammonium persulfate	Sigma	A3678; CAS: 7727-54-0
TEMED	Sigma-Aldrich	T22500; CAS: 110-18-9
Deposited Data		
Atomic mammalian respiratory supercomplex $I_1III_2IV_1$ structure	This paper	PDB: 5GUP
Mammalian respiratory supercomplex $I_1III_2IV_1$ 3-Dimensional electron microscopy density map	This paper	EMDB: EMD-9539
Software and Algorithms		
AutoEMation2	written by Jianlin Lei	jllei@tsinghua.edu.cn
Dosefgpu_driftcorr program	Li et al., 2013	http://cryoem.ucsf.edu/software/driftcorr.html
EMAN2.1	Tang et al., 2007	http://blake.bcm.edu/emanwiki/EMAN2
RELION1.4	Scheres, 2012	http://www2.mrc-lmb.cam.ac.uk/relion/index.php/Main_Page
CTFFIND3	Mindell and Grigorieff, 2003	http://grigoriefflab.janelia.org/ctf
ResMap	Kucukelbir et al., 2014	http://resmap.sourceforge.net/
COOT	Emsley et al., 2010	http://www2.mrc-lmb.cam.ac.uk/Personal/pemsley/coot
PHENIX	Adams et al., 2010	https://www.phenix-online.org/
UCSF Chimera	Pettersen et al., 2004	http://www.cgl.ucsf.edu/chimera

CONTACT FOR REAGENT AND RESOURCE SHARING

For reagents in this paper or more information about resource sharing, please contact the corresponding author Maojun Yang (maojunyang@tsinghua.edu.cn).

EXPERIMENTAL MODEL AND SUBJECT DETAILS

Animals

Fresh porcine hearts were obtained from eight- to ten-month-old male *Sus scrofa* and bought from slaughterhouse in Tsinghua University campus. All animal maintenance and experimental procedures used in current study were carried out according to guidelines of Institutional Animal Care and Use Committee (IACUC) of Tsinghua University, Beijing, China.

METHOD DETAILS

Isolation of Mitochondria from Porcine Heart

Isolation of mitochondria was carried out at 4°C. Fresh porcine heart was obtained and transported from the slaughterhouse to the laboratory as soon as possible. 100 g heart muscles were cut into small cubes, washed twice with Milli-Q water and suspended in 100 mL buffer A (100 mM Tris pH 7.4, 225 mM sorbitol, 60 mM KCl, 1 mM EGTA and 0.1% BSA). Chopped heart tissues were homogenized in a large-capacity blender for 300 s. To remove cell debris, the homogenate was centrifuged at 3,000 × *g* for 10 min. Supernatant was collected and applied to centrifugation at 20,000 × *g* for 30 min. The pellets were crude mitochondria. Crude mitochondria were suspended in 100 mL buffer B (100 mM Tris pH 7.4, 250 mM sucrose, 60 mM KCl, 40% Percoll and 0.1 mM EGTA) and centrifuged at 60,000 × *g* for 50 min. The clear mitochondrial band was aspirated carefully and diluted with buffer C (100 mM Tris pH7.4, 100 mM sorbitol, 60 mM KCl, 0.05 mM EGTA). The pure mitochondria were obtained, after the diluted sample was centrifuged for 30 min at 20,000 × *g*.

Respiratory Supercomplex $I_1III_2IV_1$ Purification

The pure mitochondria were suspended in buffer C. Respiratory supercomplexes were extracted from the mitochondrial inner membrane by 1% (w/v) digitonin overnight with slow stirring at 4 °C. An ultracentrifugation was applied at 150,000*g* for 30 min. The collected supernatant was concentrated to 1 mL by 100 kDa cutoff centrifugal filter (Millipore). Then, the 1 mL sample was loaded and centrifuged on 0.6-1.8 M sucrose gradient in buffer D (25 mM Tris, pH 7.4, 60 mM KCl, 0.1% digitonin) at 150,000*g* for 20 hr at 4°C using a SW41 rotor (Beckman). Gradients were fractionated and investigated by 3%–10% BN-PAGE gel. At last, the purified respiratory supercomplex $I_1III_2IV_1$ were concentrated and subjected to gel filtration chromatography (Superose-6 10/300 GL, GE Healthcare) in a buffer containing 10 mM Tris pH 7.4, 60 mM KCl and 0.1% digitonin. The peak fractions were collected for electron microscope.

Blue Native PAGE

Blue native PAGE technique was used to determine native respiratory supercomplexes masses. The maker in this paper was generated by digitonin-solubilized mitochondria added with 10 × loading buffer (500 mM 6-aminohexanoic acid, 5% (w/v) Coomassie brilliant blue G-250, 50% (w/v) glycerol). Chromatographically purified respiratory supercomplexes protein samples were mixed with 10 × loading buffer (0.1% (w/v) Ponceau S, 50% (w/v) glycerol) and subjected to 3%–10% blue native PAGE mini gel (1.5 × 8.3 × 7.3mm) for electrophoresis at 4°C. After the native gel electrophoresis was conducted at 150 V for 30 min, cathode buffer B (50 mM Tricine, 7.5 mM imidazole, 0.02% Coomassie brilliant blue G-250) was changed to cathode buffer B/10 (50 mM Tricine, 7.5 mM imidazole, 0.002% Coomassie brilliant blue G-250) and the running continued at 150 V for about 3 hr. All these buffers and procedures above were based on the Blue native PAGE Nature protocol (Wittig et al., 2006).

NBT Staining

Nitro blue tetrazolium (NBT) is a soluble yellow chemical compound which has two tetrazole moieties. NBT will form blue or purple precipitate formazan, when it is reduced. NBT staining is used for specific in-gel activity assays of NADH dehydrogenase (Kuonen et al., 1986). For NBT staining, BN-PAGE gels were incubated in buffer containing 100 mM Tris-glycine pH 7.4, 1 mg/ml NBT and 100 μM β-NADH for 5-10 min.

Cryo-EM Data Acquisition and Processing

4 μL aliquots of digitonin-solubilized supercomplexes at a concentration of 0.2 mg/ml were applied to glow-discharged 400-mesh Quantifoil R1.2/1.3 grids (Quantifoil, Micro Tools GmbH, Germany) coated with a home-made continuous thin layer of carbon. Grids were blotted for 1.5 s and plunged into liquid ethane using an FEI Mark IV Vitrobot operated at 4°C and 100% humidity. High-resolution images were collected on a Titan Krios microscope operated at a voltage of 300 kV with a Falcon II direct electron detector (FEI). Automated single-particle data acquisition was performed with AutoEMation (written by Jianlin Lei), with a nominal magnification of 75,000 × which yields a final pixel size of 1.08 Å at the object scale and with defocus ranging from −1.3 μm to −2.3 μm. A dose

rate on the detector was about 35 counts per pixel per second with a total exposure time of 1.5 s. Each micrograph stack contains 28 frames.

Image Processing

For Falcon II datasets processing, motion correction at micrograph level was done by the dosefgpu_driftcorr program (written by X. Li) to produce average microgrpahs over all frames (Li et al., 2013). Micrographs screening, particle picking and normalization were done with EMAN2.1 (Tang et al., 2007) and RELION1.4 (Scheres, 2012). All particles were selected half-manually. The boxing tool 'Swarm' (EMAN2.0) was used to get coordinate files with the suffix 'box'. The particle diameter was set to 380 pixels, and proximity threshold was set to 2.3 to get as many particles as possible. Particles were then extracted using Relion 1.4 with a box size of 480 pixels. Program of CTFFIND3 (Mindell and Grigorieff, 2003) was used to estimate the contrast transfer function parameters. The 2D, 3D classification and refinement were performed with RELION. 424,002 particles from 4,660 micrographs were subject to a cascade of 2D and 3D classification. 349k particles were selected after three rounds of 2D classification. Two rounds of 3D classification were then performed with these particles. Different combinations of particles from these classes were tested in refinement. After 3D classification, a set of relatively homogeneous particles (161,912) were subjected to the final refinement, with the 5.4 Å model (PDB: 5GPN) low-pass filtered to 60 Å as initial reference. The refinement resulted in an overall structure at a resolution of 6.6 Å, with regions defined by the soft mask being 4.2 Å. A second round of refinement was done by applying an enlarged soft mask of the supercomplex, and improved the resolution to 4.0 Å. The masked refinement procedure was performed to improve the local resolution of our density map. We use Relion software to prepare soft masks. The threshold was set to 0.005. The initial binary mask is extended 3 pixels in all directions, and is further extended with a raised-cosine soft edge of the 5 pixels width. Carefully modified soft masks for supercomplex $I_1III_2IV_1$, supercomplex I_1III_2, complex I, complex III and complex IV were applied to the particle images in 3D autorefinement process, respectively, giving a better resolution of 4.0 Å, 3.9 Å, 3.6 Å, 3.6 Å and 6.4 Å for each subregion, respectively. The 162k particles were further classified into two subsets with different conformations (defined as state I and state II) by 3D classification. Each class contains 80k (state I) and 82k (state II) particles. Both classes were subjected to the 3D refinement. The overall resolutions of the two structures were 4.5 Å (state I) and 4.6 Å (state II), respectively.

Model Building and Refinement

To build atomic models of CI, we used 4.0 Å porcine CI structure (PDB code: 5GPN) (Guo et al., 2016) as the initial model. With improved 3.6 Å higher resolution, we were able to model side chains and local geometry to higher accuracy. CI models were adjusted and real-space refined using COOT (Emsley et al., 2010). Finally, the polypeptides of 14 core subunits and 30 supernumerary subunits were assigned into the 3.6 Å density map. As for atomic models of CIII, 4.0 Å porcine CIII structure (Guo et al., 2016) was chosen as the initial template and the new CIII model was built and refined in the same way as CI. All ligands and phospholipids models were generated using elbow (Moriarty et al., 2009) module in PHENIX (Adams et al., 2010) by their geometric constraints. The ligands and phospholipids were docked into densities and refined using COOT. All the figures were created by UCSF Chimera (Pettersen et al., 2004).

QUANTIFICATION AND STATISTICAL ANALYSIS

All reported resolutions are based on the gold-standard FSC = 0.143 criteria (Scheres and Chen, 2012), and the final FSC curve were corrected for the effect of a soft mask using high-resolution noise substitution (Chen et al., 2013). FSC curves of the final model versus the summed map and half maps were calculated with the soft-ware written by X, Li. Final density maps were sharpened by B-factor of -200 Å^2 using RELION. Local resolution map was calculated using ResMap (Kucukelbir et al., 2014). And the models with the ligands and phospholipids were subjected to global refinement and minimization in real space refinement using PHENIX.

DATA AND SOFTWARE AVAILABILITY

Different types of software we used to process cryo-EM data and build structure model were reported in Method Details and indicated in Key Resources Table. The accession number for the atomic coordinate and the corresponding map of the *Sus scrofa* respiratory supercomplex $I_1III_2IV_1$ reported in this paper is the Worldwide Protein Data Bank (http://www.rcsb.org): 5GUP, and the Electron Microscopy Data Bank (http://emdatabank.org): EMD-9539, respectively. The corresponding map has been deposited in the Electron Microscopy Data Bank with the accession codes EMD-9539.

Cell

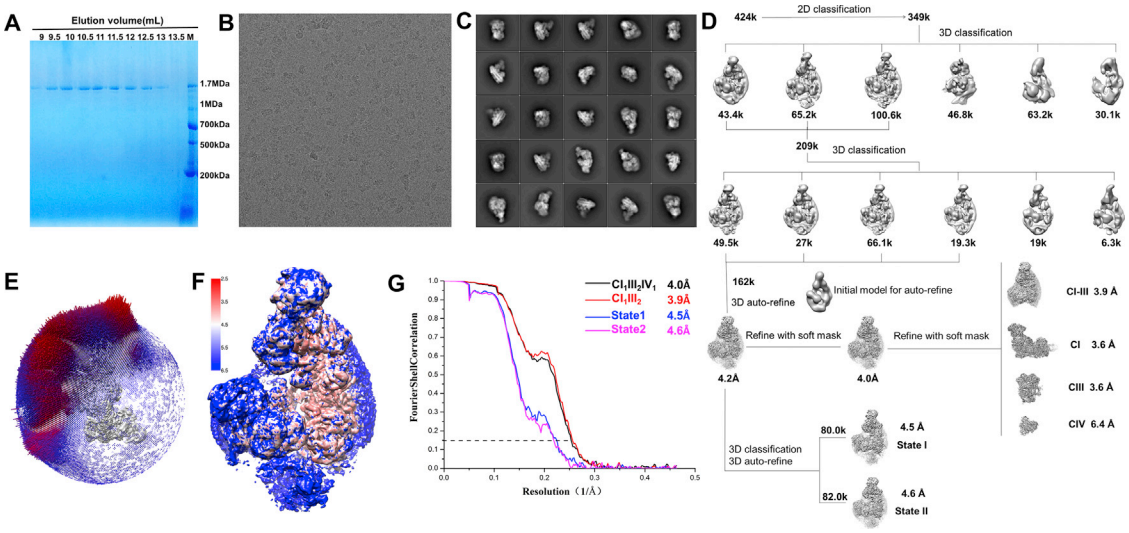

Figure S1. Cryo-EM Analysis of $SCI_1III_2IV_1$, Related to Figure 1 and STAR Methods

(A) Protein samples of the size-exclusion chromatography fractions by Superose-6 (10/300 GL) column were subjected to BNPAGE. Fractions of 9.5-10 mL (elution volume) were used for negative staining EM and cryo-EM.

(B) A representative cryo-EM micrograph of the $SCI_1III_2IV_1$.

(C) Representative 2D class averages of different views show fine features of the F-shaped structure.

(D) Workflow of 3D reconstruction with cryo-EM data. 349,000 particles were kept after 2D classification, and subject to two rounds of 3D classification. A final dataset containing ~162,000 particles were used for high-resolution refinement and soft masks refinement in different regions (see methods for more details). The ~162,000 particles were subjected to another round of 3D classification and auto-refine to 4.5 and 4.6 Å, respectively, in two states.

(E) Particle orientation distributions in the last iteration of the structural refinement. Red cylinders mean more particles on these orientations. Heights of cylinders represent the relative numbers of particles.

(F) Local resolution map of the final 3D density map. Viewed from the matrix region.

(G) Gold-standard Fourier Shell Correlation (FSC) curve of the final density maps, after correction of the soft-mask-induced effects. The final resolution of $SCI_1III_2IV_1$ and SCI_1III_2 are 4.0 and 3.9-Å, respectively.

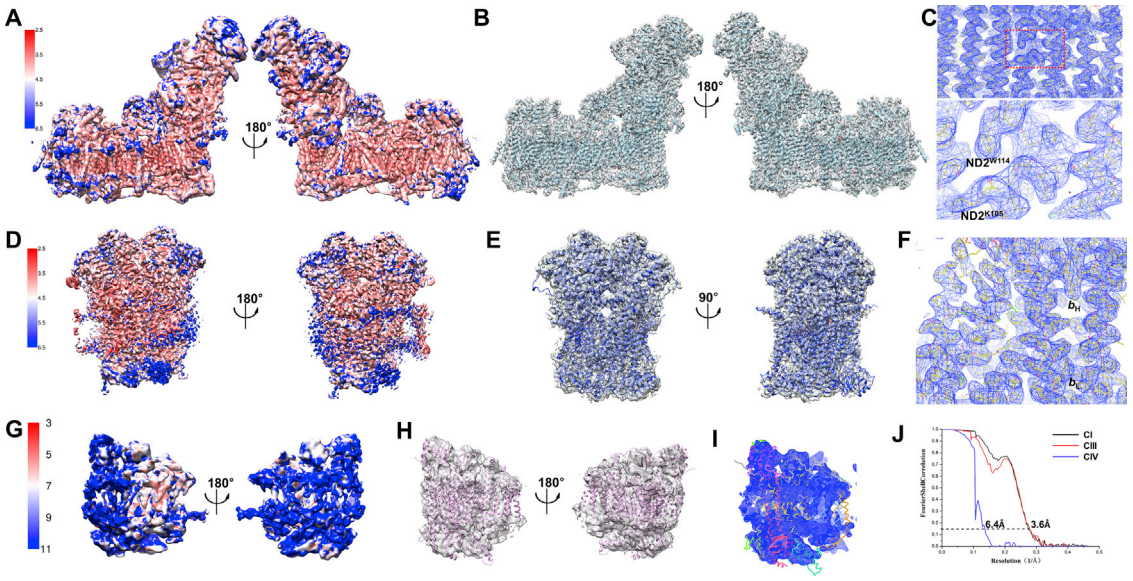

Figure S2. Statistics of the Final Density Map of CI, CIII, and CIV after Soft Mask Refinement, Related to Figures 1 and 2 and STAR Methods

(A) Local resolution maps of the final 3D density map of CI. Viewed in two differently rotated views alone the membrane.

(B) The model of CI is fitted into the density map. Viewed in two differently rotated views alone the membrane. The figures are generated in Chimera.

(C) The density map (blue meshes) of the transmembrane region of CI is displayed at rmsd = 12 contour level. The bottom panel shows the density of the region of the red dash line rectangle. The backbone is shown in line in Coot.

(D) Local resolution maps of the final 3D density map of CIII. Viewed in two differently rotated views alone the membrane.

(E) The model of CIII is fitted into the density map. Viewed in two differently rotated views alone the membrane. The figures are generated in Chimera.

(F) The density map (blue meshes) of the transmembrane region of CIII is displayed at rmsd = 12 contour level. The heme molecules of b_H and b_L are indicated. The backbone is shown in line in Coot.

(G) Local resolution maps of the final 3D density map of CIV. Viewed in two differently rotated views alone the membrane.

(H) The model of CIV is fitted into the density map. Viewed in two differently rotated views alone the membrane. The figures are generated in Chimera.

(I) The density map (blue meshes) of the CIV is displayed at rmsd = 10 contour level. The structure of CIV is shown in line with different subunits in different colors in Coot.

(J) Gold-standard Fourier Shell Correlation (FSC) curves of the final density map, after correction of the soft-mask-induced effects. The final resolution of CI, CIII and CIV are 3.6, 3.6 and 6.4 Å, respectively.

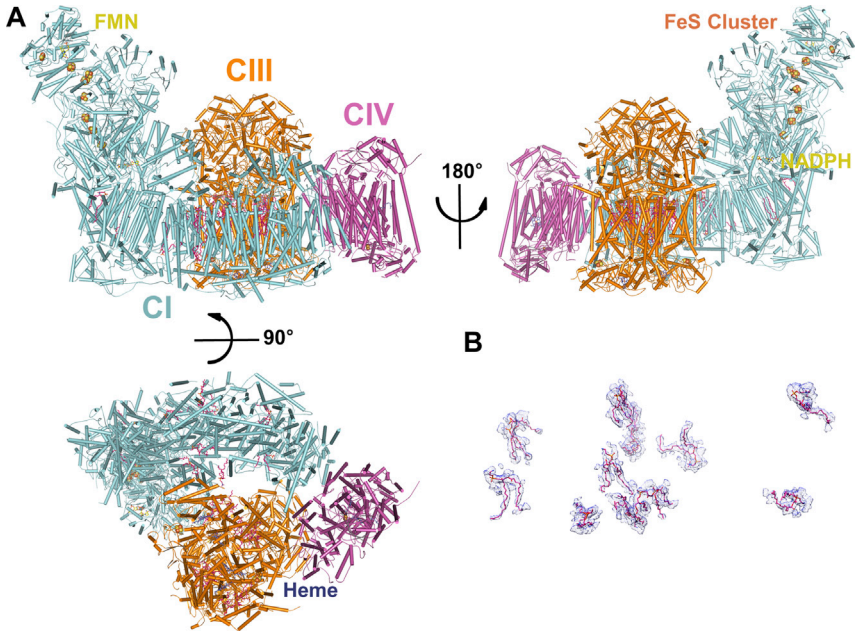

Figure S3. The Overall Structure of $SCI_1III_2IV_1$, Related to Figures 1 and 2

(A) The overall structure of $SCI_1III_2IV_1$. Cartoon representation of the $SCI_1III_2IV_1$ structure in three differently rotated views along the membrane. The complexes are colored as labeled with texts in the same colors, respectively.

(B) The electron density of lipid molecules in the CI structure (7σ contour level). The figure is made in Chimera.

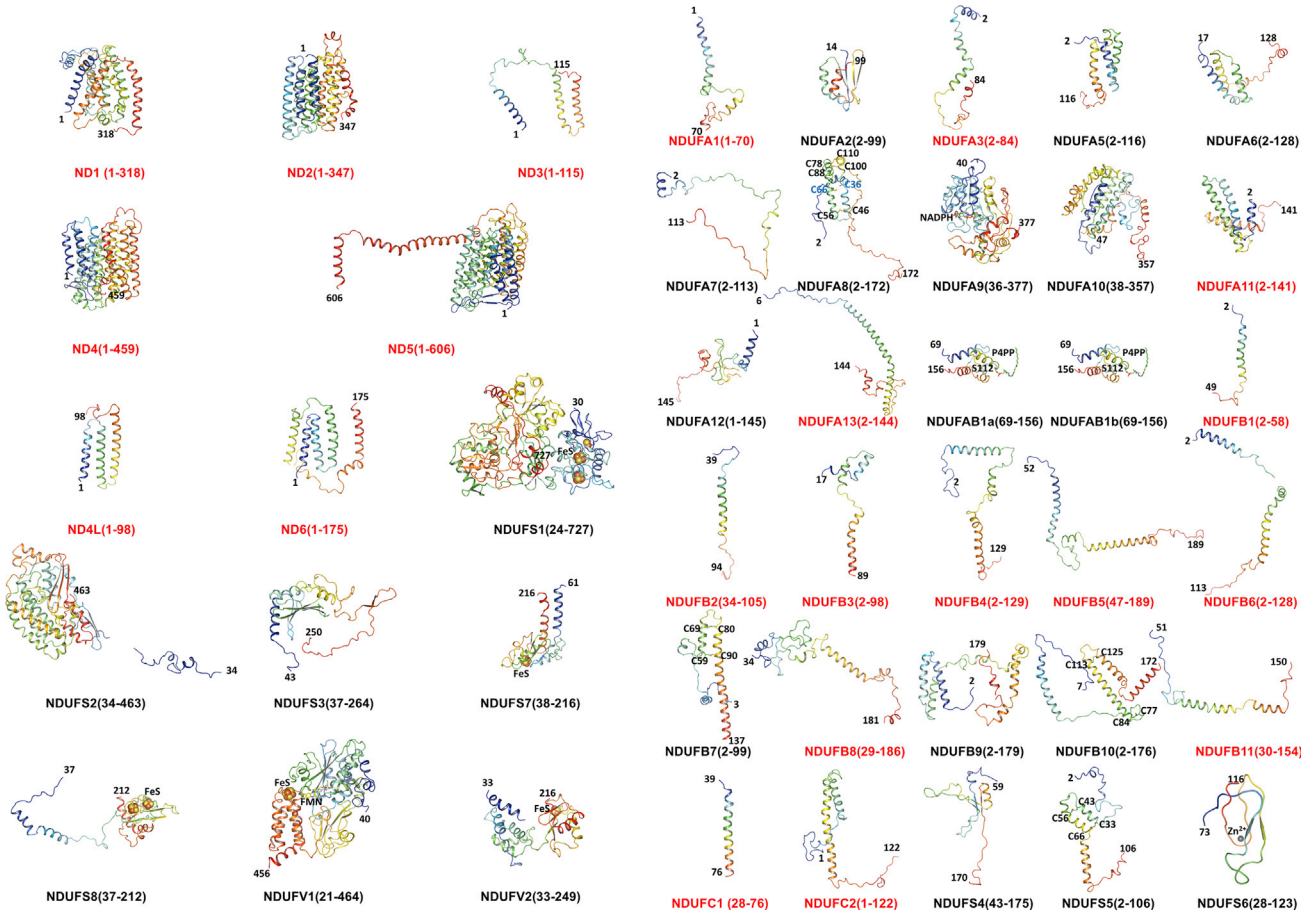

Figure S4. Structures of Individual Subunits of *Sus scrofa* CI Subunits, Related to Figure 2

3D structures of *Sus scrofa* CI individual subunits. The N- and C-termini are indicated in the structures, and matured protein residue numbers are shown in brackets. The membrane proteins are marked in red. The cofactors are shown in sticks. The Fe-S clusters are shown in spheres.

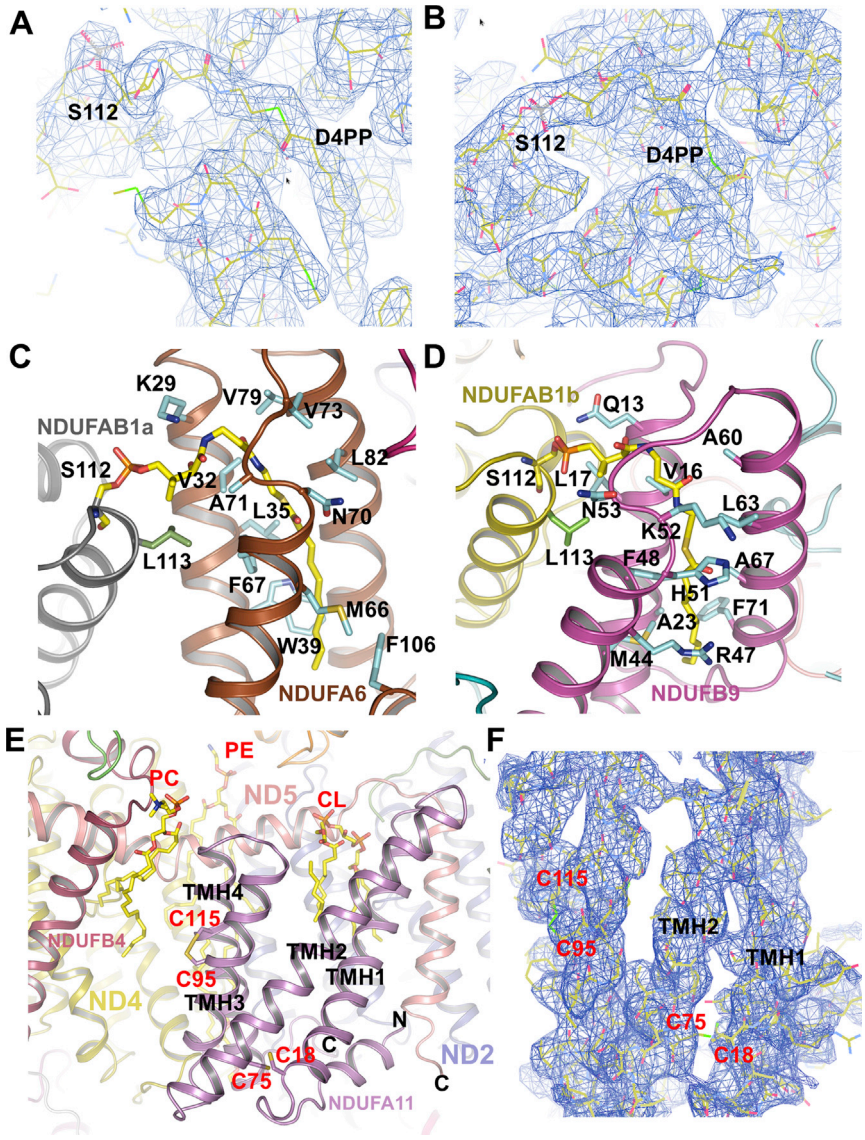

Figure S5. D4PP or Phospholipids Molecules Mediate the Protein-Protein Interactions of CI, Related to Figures 2 and 5

(A) The electron density map (blue meshes) of the decanoyl (C10)-4'-phosphopantetheine (D4PP) group in NDUFA6 is displayed at rmsd = 12 contour level. The backbone is shown in line. The figure was prepared in Coot.

(B) The electron density map (blue meshes) of the D4PP group in NDUFB9 is displayed at rmsd = 12 contour level. The backbone is shown in line. The figure was prepared in Coot.

(C) Cartoon represent of the D4PP interaction in the NDUFAB1a-NDUFA6 complex. The phosphorylated NDUFAB1a^{S112} and the linked D4PP are shown in yellow sticks. The residues that interact with the D4PP are shown in sticks and indicated.

(D) Cartoon represent of the D4PP interaction in the NDUFAB1b-NDUFB9 complex. The phosphorylated NDUFAB1b^{S112} and the linked D4PP are shown in yellow sticks. The residues that interact with the D4PP are shown in sticks and indicated.

(E) Cartoon represent of the NDUFA11. Viewed along the membrane. The side chain of Cys18 and 75 direct to different position, while the Cys95 forms a disulfide bond with Cys115. The backbones of the phospholipid molecules are shown in yellow lines. The proteins that interact with NDUFA11 are colored individually and labeled with texts in the same colors. Viewed along the membrane.

(F) The electron density map (blue meshes) of NDUFA11 is displayed at rmsd = 12 contour level. The backbone is shown in line. The figure was prepared in Coot.

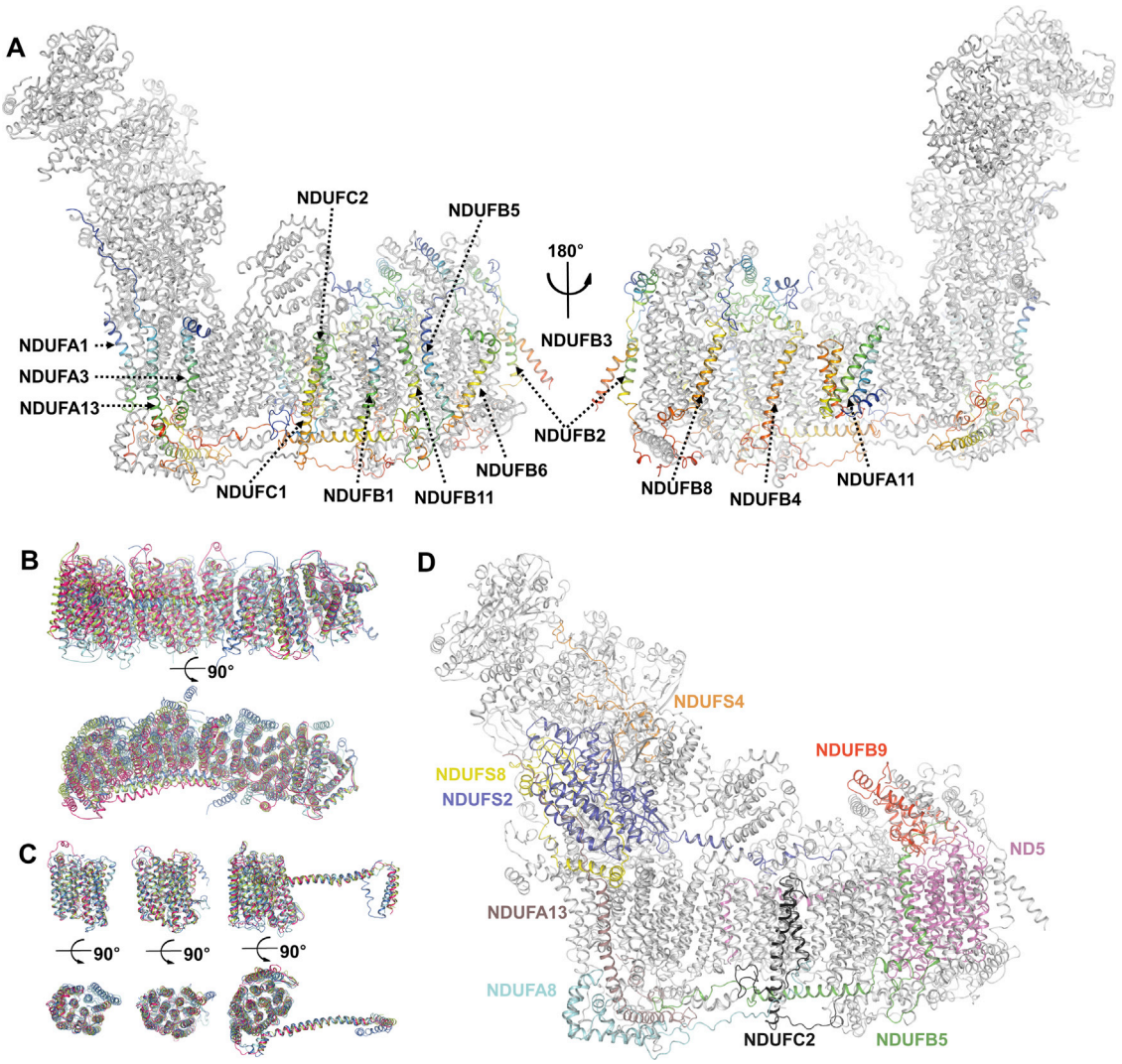

Figure S6. The Structural Characters of CI, Related to Figures 2, 3, and 6

(A) All these C-termini of the transmembrane containing supernumerary subunits are located in the IMS.CI is in two differently rotated views along the membrane. The 14 transmembrane supernumerary subunits are shown in cartoon and colored in rainbow. The blue and red ends of every subunit stand for the N- and C-termini, respectively.

(B) The conformational changes of the core subunits forming membrane arms in different species. The structures of membrane core subunits from *T. thermophiles* (cyan, PDB accession 4HEA), *Y.lipolytica* (marine, PDB accession 4WZ7) and *B.taurus* (limon PDB accession 4UQ8) have been superimposed separately by their corresponding ND1 subunits on the subunits from *S. scrofa* (hot pink). These subunits are viewed from the side (along the membrane) and from the top (matrix side).

(C) The structures of the core subunits are similar to each other in different species. The comparison of the ND2, ND4 and ND5 core subunits from different species shown in the same way as panel A.

(D) NDUFA8, NDUFA13, NDUFB5, NDUFB9, NDUFB10, NDUFS2, NDUFS4, NDUFS8 and ND5 colored and labeled in the same colors form intensive interactions with other subunits and hold CI as an integral complex. Viewed along the membrane.

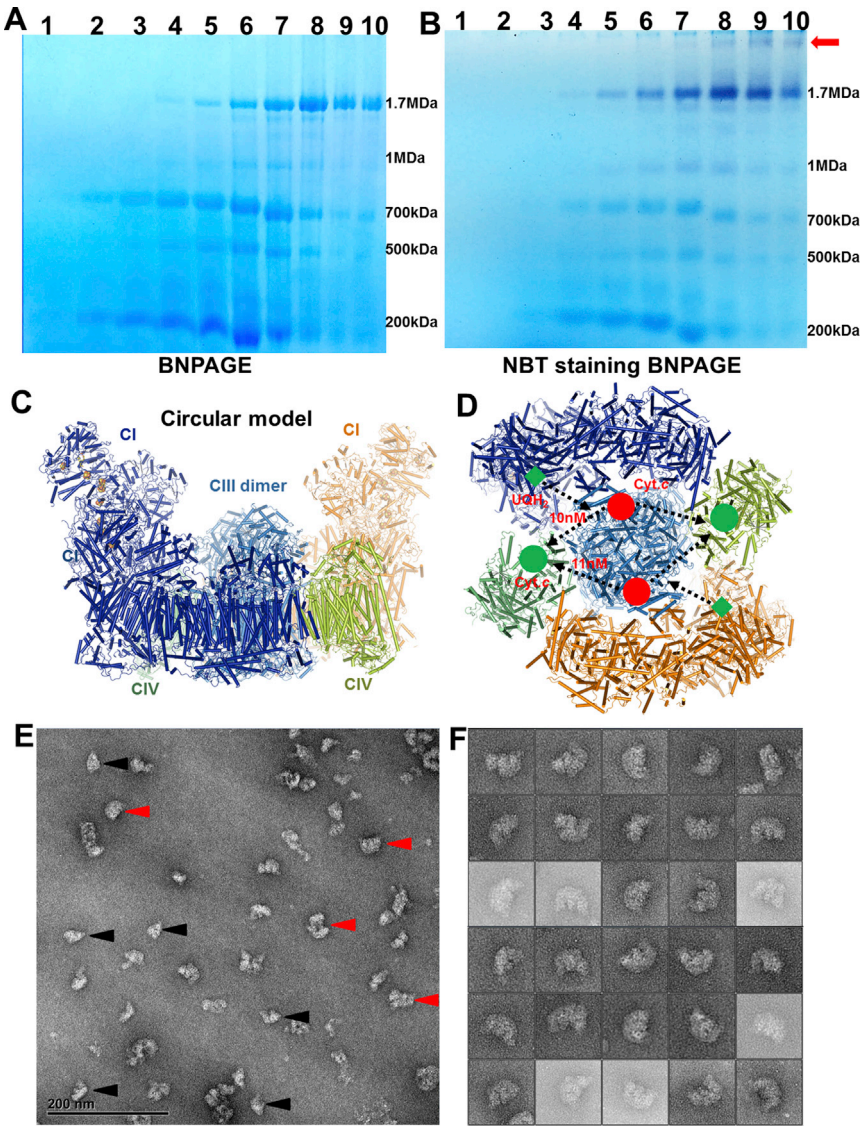

Figure S7. The Supercomplex Could Form Supra-supercomplexes, Related to Figure 5 and STAR Methods

(A) Fractions of sucrose gradient ultracentrifugation were analyzed by BNPAGE.

(B) In-gel staining of the native gel by NBT (The protein samples were the same as panel A, but the gels were two different gels). Higher molecular weight bands were indicated by a red arrow.

(C) Cartoon representation of the circular model of the $SCI_2III_2IV_2$. Viewed along the membrane. The complexes are colored as texts labeled.

(D) The possible pathways of Cyt.*c* transfer in the circular model. The UQ is reduced in CI by NADH through a series of electron transfer pathways and UQH_2 (green square) could diffuse to the CIII to reduce the Cyt.*c* (red disk). The reduced Cyt.*c* (green disk) could be transferred in two directions to two neighboring CIV about the same distance (~10-11 nM).

(E) Micrograph of negatively stained samples purified from the fractions as shown in Figure S1B. The $SCI_1III_2IV_1$ particles are indicated with black arrowheads and the circular supra-supercomplex particles are indicated with red arrowheads.

(F) A collection of particles representing the supra-supercomplex. The shape and size suggest the supra-supercomplex particles are in the arrangement of $SCI_2III_2IV_2$.